# Observations of mantle seismic anisotropy using array techniques: shear-wave splitting of beamformed SmKS phases

**Jonathan Wolf[1], Daniel A. Frost[2], Maureen D. Long[1], Edward Garnero[3], Adeolu O. Aderoju[3], Neala Creasy[4,5], Ebru Bozdag[4]**

[1]Department of Earth and Planetary Sciences, Yale University, New Haven, CT, USA
[2]Department of Earth and Planetary Sciences, University of California, Berkeley, CA, USA
[3]School of Earth and Space Exploration, Arizona State University, Tempe, AZ, USA
[4]Colorado School of Mines, Golden, CO, United States
[5]Los Alamos National Laboratory, Los Alamos, NM, USA

**Key Points:**

- Major limitations for shear-wave splitting measurements are the limited number of suitable phases and low signal-to-noise ratios.
- Beamforming enhances the signal-to-noise ratio, enabling us to use unusual seismic phases and a larger data fraction for shear-wave splitting measurements.
- This holds potential for investigations of mantle anisotropy, particularly in the lowermost mantle.

Corresponding author: Jonathan Wolf, `jonathan.wolf@yale.edu`

## Abstract

Shear-wave splitting measurements are commonly used to resolve seismic anisotropy in both the upper and lowermost mantle. Typically, such techniques are applied to SmKS phases that have reflected (m-1) times off the underside of the core-mantle boundary before being recorded. Practical constraints for shear-wave splitting studies include the limited number of suitable phases as well as the large fraction of available data discarded because of poor signal-to-noise ratios (SNRs) or large measurement uncertainties. Array techniques such as beamforming are commonly used in observational seismology to enhance SNRs, but have not been applied before to improve SmKS signal strength and coherency for shear wave splitting studies. Here, we investigate how a beamforming methodology, based on slowness and backazimuth vespagrams to determine the most coherent incoming wave direction, can improve shear-wave splitting measurement confidence intervals. Through the analysis of real and synthetic seismograms, we show that (1) the splitting measurements obtained from the beamformed seismograms (beams) reflect an average of the single-station splitting parameters that contribute to the beam; (2) the beams have (on average) more than twice as large SNRs than the single-station seismograms that contribute to the beam; (3) the increased SNRs allow the reliable measurement of shear wave splitting parameters from beams down to average single-station SNRs of 1.3. Beamforming may thus be helpful to more reliably measure splitting due to upper mantle anisotropy. Moreover, we show that beamforming holds potential to greatly improve detection of lowermost mantle anisotropy by demonstrating differential SKS-SKKS splitting analysis using beamformed USArray data.


## Plain Language Summary

When earthquakes occur, seismic waves are produced that travel through the deep Earth to distant seismic stations. In some portions of the Earth, seismic waves travelling in different directions or with different vibration directions travel at different speeds. This phenomenon is known as seismic anisotropy and results from individual mineral crystals aligning with mantle flow. Therefore, by measuring seismic anisotropy, we can obtain insights into how Earth's mantle flows, a process called mantle convection.

In this work, we show that seismic anisotropy can be inferred from recordings of seismic phases that are summed (or stacked) across a number of spatially separated sta-

tions (seismic arrays). The resulting stacks are also called beams. Beams have an increased signal clarity compared to single-station seismograms, leading to several advantages for analyses of seismic anisotropy. For example, the increased signal strength in beams allows for the usage of weaker seismic phases, which are not commonly used for measuring seismic anisotropy. Moreover, measurements made on beamformed data are more robust. This new technique enables us to suggest new directions for lowermost mantle anisotropy analyses.

## 1 Introduction

Measurements of seismic anisotropy, or the dependence of seismic velocities on the propagation direction and polarization of the wave, may reveal flow and deformation within the Earth (e.g., Montagner & Anderson, 1989; Marone & Romanowicz, 2007; Russo et al., 2010; Long & Becker, 2010; Nowacki et al., 2010; Walpole et al., 2014; Creasy et al., 2017; Grund & Ritter, 2018; Wolf et al., 2019; Wolf & Long, 2022). Measurements of upper and lowermost mantle anisotropy can yield relatively direct constraints on mantle convection and dynamics; in contrast, the bulk of the lower mantle is almost isotropic (e.g., Panning & Romanowicz, 2006). In general, the fast polarization directions of upper mantle anisotropy often align with plate motions (e.g., Silver, 1996; Chang et al., 2014; Becker & Lebedev, 2021), although there are some notable exceptions (e.g., Kneller et al., 2005). Spatially averaged patterns of upper mantle anisotropy inferred from surface and body waves are similar (e.g., Becker & Lebedev, 2021). In cases of particularly good ray coverage, details of upper mantle mineralogy and olivine fabric types have even been inferred from measurements of upper mantle anisotropy (e.g., Löberich et al., 2021).

While upper mantle anisotropy is relatively straightforward to infer, lowermost mantle anisotropy is more challenging, both from a measurement (e.g., Wookey et al., 2005b; Nowacki & Wookey, 2016; Tesoniero et al., 2020; Wolf et al., 2022a, 2022b) and interpretation (e.g., Ford et al., 2015; Creasy et al., 2020; Wolf & Long, 2022) point of view. Reasons include that the the upper mantle influences the seismic phases that are commonly used to infer lowermost mantle anisotropy, and the mechanism for lowermost mantle anisotropy remains imperfectly understood (e.g., Wookey et al., 2005a; Nowacki et al., 2011). Lowermost mantle anisotropy is thought to be particularly strong at the edges of the two antipodal large-low velocity provinces (LLVPs) atop the core-mantle boundary (e.g., Wang & Wen, 2004; Cottaar & Romanowicz, 2013; Deng et al., 2017; Reiss et

al., 2019). Anisotropy at the base of the mantle has also been connected to slab-driven flow in lowermost mantle regions with faster than average seismic velocities (e.g., Nowacki et al., 2010; Asplet et al., 2020; Creasy et al., 2021; Wolf & Long, 2022) and to upwelling flow in the deep mantle at the base of plumes (e.g., Ford et al., 2015; Wolf et al., 2019). Inferring flow patterns at the base of the mantle remains challenging, however, due to the scarcity of suitable waveforms, large measurement uncertainties, and/or insufficient data coverage (Wookey et al., 2005b; Nowacki et al., 2010; Creasy et al., 2017; Wolf et al., 2019; Wolf & Long, 2022). Improving our ability to measure lowermost mantle anisotropy will be beneficial for answering several outstanding big-picture questions related to deep mantle dynamics. For example, more detailed knowledge about deep mantle anisotropy may potentially help us to understand the origin and evolution of the LLVPs (e.g., Torsvik, 2019; Wolf & Evans, 2022), the fate of subducted slabs (e.g., van der Hilst et al., 1997; Tackley, 2000), and patterns of whole mantle convection (e.g., Bercovici & Karato, 2003; Li & Zhong, 2017).

Shear-wave splitting measurements are commonly applied to SKS phases (Figure 1a) to characterize upper mantle anisotropy beneath a station (e.g., Long et al., 2009; Liu et al., 2014; Walpole et al., 2014). SKS is a convenient target phase because it is initially SV polarized due to the P-to-SV conversion at the core-mantle boundary (CMB) on the receiver-side leg of the raypath. SKS splitting measurements have been applied to a large number of stations world-wide and are available in open access databases (Barruol et al., 2009; Trabant et al., 2012; Liu et al., 2014). Results reported in these databases represent a collection of the well-constrained measurements that could be obtained, while a substantial fraction of measurements that are of poor quality are not included. The most common reason to discard data in SmKS splitting studies is large measurement confidence intervals due to poor waveform clarity or low signal-to-noise ratios (SNRs). This means that only a relatively small subset of potentially useful SKS splitting data is used for geologic interpretation. The same is true for other commonly used phases such as SKKS (Figure 1a) and PKS, that are also sometimes suitable to measure upper mantle anisotropy.

The splitting of *KS (e.g., SKS, PKS, SKKS, etc.) phases is generally thought to mostly reflect upper mantle anisotropy because the upper mantle is likely more strongly anisotropic than the deep mantle (e.g., Panning & Romanowicz, 2006). However, in some cases, there may be some contribution from anisotropy in the deeper mantle. The pres-

ence of lowermost mantle anisotropy is often inferred from differential SKS-SKKS splitting (e.g., Niu & Perez, 2004; Restivo & Helffrich, 2006; Long, 2009; Long & Lynner, 2015; Deng et al., 2017; Grund & Ritter, 2018; Wolf et al., 2019; Reiss et al., 2019; Lutz et al., 2020; Asplet et al., 2020). The argument for this analysis technique is that SKS and SKKS raypaths are very similar in the upper mantle, but they sample different portions of the deep mantle and have different propagation directions (see Figure 1a). Therefore, significant differences in SKS and SKKS splitting can be attributed to a contribution from anisotropy in the deep mantle to the splitting of one or both phases. A downside of this technique is that it requires the measurements of well-constrained SKS and SKKS splitting parameters on a single seismogram, a quality requirement often only met by a small subset of data. Additionally, measurements of differential SKS-SKKS splitting often show substantial scatter (e.g., Wolf et al., 2019; Reiss et al., 2019; Lutz et al., 2020; Asplet et al., 2020) and are therefore not straightforward to interpret.

Stacking of seismic data is commonly applied to increase SNRs based on the assumption that the seismic phase is coherent and so will sum constructively, while the background noise will be incoherent and will sum destructively. However, stacking approaches are applied in shear-wave splitting studies relatively rarely. Wolfe and Silver (1998) introduced the stacking of single-station splitting error surfaces, which is based on the assumption of single layer seismic anisotropy with shear-wave splitting that is largely independent of the backazimuth. Such an approach has been extended to multiple layers and been applied to station arrays (e.g., Link & Rümpker, 2021). Moreover, two recent studies of deep mantle anisotropy have applied a linear stacking approach to seismic data recorded across an array of seismic stations (Wolf & Long, 2022; Wolf et al., in review) and then measured splitting of SKS, SKKS and $S_{diff}$ waveforms from the resulting stacks. However, previous work that incorporated stacking across multiple stations has relied on restrictive assumptions that are often specific to the dataset in question.

One promising technique is beamforming, which has been shown to be suitable for stacking and amplifying low amplitude signals (e.g., Rost & Thomas, 2002, 2009; Frost et al., 2013). Beamforming is commonly used in studies of mantle structure (e.g., Frost et al., 2020; Frost & Romanowicz, 2021; Li et al., 2022); however, it has not to our knowledge been applied before to shear-wave splitting. We use a beamforming method based on slowness and backazimuth vespagrams to determine the incoming wave direction which stacks most constructively and produces a coherent beam (Section 3.1). Applying a beam-

forming approach is a potentially interesting avenue for improving measurements of mantle seismic anisotropy, and may be particularly promising for studies of anisotropy in the deep mantle. Beamforming increases SNR and waveform clarity, allowing the use of a larger data fraction in shear-wave splitting studies and yield datasets with substantially less scatter. Additionally, a beamforming approach may allow the use of unusual phases that normally have amplitudes that are too low in single-station seismograms to be used in splitting studies (for example, S3KS phases).

The aim of this study is to establish the application of shear-wave splitting measurements to beamformed data as a viable tool for measuring mantle anisotropy. In what follows, we detail our dataset and basic data processing (Section 2), our beamforming and shear-wave splitting measurement approaches (Section 3) and show that we can measure differential splitting between pairs of phases using a beamforming approach (Section 4). Then, we analyze shear-wave splitting of both beams and the single-station seismograms used to form the beams (Section 5.1). We do this without making assumptions where along the raypath the seismic anisotropy is located. Most waves are likely primarily influenced by upper mantle anisotropy; however, for some measurements, there may be a lowermost mantle anisotropy contribution. We also inform our conclusions through the analysis of synthetic data generated for a series of simple anisotropic models using the AxiSEM3D (Leng et al., 2016, 2019) global wavefield modeling tool (Section 5.2). Finally, we show a proof-of-concept example in which we compare SKS-SKKS differential splitting measured from beamformed and single station data, investigating the lowermost mantle beneath the eastern Pacific Ocean (Section 6). We find that measurements of SKS-SKKS differential splitting from beams are substantially more robust than from single-station seismograms, establishing a potentially useful approach for improving studies of anisotropy at the base of the mantle.

## 2 Data

We use velocity seismograms from 8 earthquakes beneath the western Pacific Ocean (Supplementary Table S1) to analyze beam splitting parameters. These events are selected because they possess clear SKS and SKKS phases across a large number of seismic stations. We use the stations of the USArray and construct subarrays of subsets of stations drawn from the whole array. Figure 1b shows the source-subarray configuration used in this study. The data coverage across the United States (see Figure 1b, zoom-in)

is mainly influenced by the regions in which USArray stations were operating at the time when these 8 events occurred. We select events in part to ensure that our measurements cover different tectonic settings across the United States. Our subarrays, cover the Cascadia subduction zone and subduction zone backarc as well as the California transform boundary. We also use a large swath of stations in the continental interior; these stations potentially sample anisotropy frozen in the old and stable lithosphere. We thus include a variety of inferred upper mantle splitting patterns. For example, shear-wave splitting caused by anisotropy in old continental lithosphere is generally weak to moderate (e.g., Chen et al., 2021) and splitting patterns in the US continental interior exhibit lateral heterogeneity (Yang et al., 2017). Splitting patterns in the Cascadia subduction zone are complex (e.g., Long, 2016), but the complex Cascadia backarc exhibits nearly uniform fast polarization directions with delay times that are generally large ($\sim$2 s but with substantial variability (e.g., Long et al., 2009; Eakin et al., 2019).

## 3 Methods

### 3.1 Beam forming

For each event, we collect three component velocity data and then rotate the east and north components to radial (R) and transverse (T) components relative to the great circle path between events and stations. We construct subarrays of between 10 and 20 USArray stations and beamform the traces, and then record the slowness and back azimuth for which the SmKS beam amplitude is maximal, following the method of Frost et al. (2020). The beam is calculated at the "beam point", which we set to the arithmetic average location of all stations in the subarray. The beam point is also used as the reference from which to calculate the distance and backazimuth to the source.

When an SmKS phase reflects off the underside of the CMB, the waveform undergoes a $\frac{\pi}{2}$ phase shift for every underside reflection (Choy & Richards, 1975), similar to S waves reflected off the surface of the Earth (e.g., SS, SSS, etc.). To correct for this, we apply a Hilbert transform to every SmKS wave (where $m \geq 2$) for each underside reflection, so its phase is comparable to SKS.

For each complete subarray, we stack each of the radial and transverse separately for the different SmKS phases that are predicted to arrive at that source-receiver distance. We calculate predicted arrival times using the using 1D reference model PREM

(Dziewonski & Anderson, 1981) and the TauP toolkit (Crotwell et al., 1999). Each SmKS phase is stacked separately, due to the differences in slownesses and backazimuths for different phases. We window data 40 s prior to and 40 s after the predicted arrival times of the SmKS wave. We then construct vespagrams by simultaneously grid searching over slownesses (from 0 to 9 s/° in 0.1 s/° increments) and backazimuths (±20° in 1° increments relative to the great-circle path) and then correct for the moveout for that slowness and backazimuth (Davies et al., 1971), as illustrated in Figure 2. We use a curved wavefront approach, which is appropriate for larger arrays such as those used here, instead of the typical plane-wave approximation (e.g., Rost & Thomas, 2009). To ensure that we construct the most coherent beam, we improve the slowness and backazimuth resolution using a coherence measure called the F-statistic (Selby, 2008; Frost et al., 2013), which measures the degree of similarity of all the individual traces to the beam calculated in a moving time window to produce an F-trace. For each phase, we select the slowness and backazimuth that corresponds to the maximum amplitude in F-trace at the time of the SmKS wave and re-construct the linearly stacked beam (without the F-statistic) for this incoming wave direction. The result is three component beams for each subarray computed across the whole of the regional array.

For data processing, we bandpass-filter the data, retaining periods between 4-50 s. This period range effectively highlights SmKS relative to the noise to determine slowness and backazimuth of the incoming wave as described above. These slowness and backazimuth values are then used to stack unfiltered and unnormalized data, so that subsequent splitting measurements are not affected by this preprocessing.

### 3.2 Shear-wave splitting measurements

Splitting measurements are conducted on single-station and beamformed data using the SplitRacer software (Reiss & Rümpker, 2017; Reiss et al., 2019), a MATLAB-based graphical user interface. We retain periods between 6-25 s, which is a commonly used range (e.g., Wolf et al., 2022a). SplitRacer uses an algorithm that automatically picks the analyzed time windows and then retrieves splitting parameters for each time window individually; this ensures that the measured splitting parameters are robust and do not depend on the specific choice of the time window. SplitRacer calculates the time lag between slow and fast quasi S waves ($\delta t$) and the fast polarization direction ($\phi$, measured clockwise from the north) using the transverse energy minimization technique (Silver

& Chan, 1991). We calculate 95% confidence intervals using a corrected error estimate algorithm (Walsh et al., 2013). From the fast direction $\phi$, we also calculate $\phi'$, which denotes the fast polarization measured clockwise from the backazimuthal direction (e.g., Nowacki et al., 2010). We also use SplitRacer to estimate the splitting intensity (Chevrot, 2000), $SI$, defined as

$$SI = -2\frac{T(t)R'(t)}{|R'(t)|^2} \approx \delta t \sin(2(\alpha - \phi)) \ , \tag{1}$$

where R(t) is the radial component, $R'(t)$ is the radial component time derivative, $T(t)$ is the transverse component and $\alpha$ is the wave's initial polarization. This measurement is based on the waveform similarity between the transverse component, $T(t)$, and the radial component time derivative, $R'(t)$, and quantifies how much energy is partitioned from the radial to the transverse component via splitting. Similarity between the transverse component and the radial component time derivative is expected in case of splitting due to seismic anisotropy if the dominant period is much smaller than the time delay $\delta t$ (Silver & Chan, 1991; Chevrot, 2000).

We measure splitting parameters ($\phi$, $\delta t$, $SI$) for single-station records and beam traces for subarrays across USArray. An example set of measurements is shown in Figure 3 for an event that occurred on 2011/12/14 (Supplementary Table 1) at a subarray located in the southern US. We show individual transverse and radial waveforms, sorted as a function of epicentral distance and aligned with respect to the expected SKS phase arrival according to the predictions of PREM. We also demonstrate transverse and radial component beams along with the diagnostic splitting outputs from SplitRacer. The fast polarization direction ($\phi$ or $\phi'$) and the time delay ($\delta t$) are both well-constrained. The particle motion of the beam is elliptical, as would be expected for a wave that has undergone splitting. After correcting for the best-fitting splitting parameters, the corrected particle motion is almost perfectly linear and the energy on the transverse component is minimized.

## 4 Retrieval of SmKS beam splitting parameters for multiple phases

We first demonstrate that we can successfully retrieve splitting parameters from beamformed data for multibounce SmKS phases for an example event-subarray configuration. We show results for an event that occurred on 2010/07/29 (Supplementary Ta-

ble S1). We present waveforms and SplitRacer diagnostic plots for SKS (panel a), SKKS (b) and S3KS (c) phases in Figure 4. The radial waveforms of the three phases do not look exactly alike, as would be theoretically expected after applying the appropriate number of Hilbert transforms (Section 3.1). However, for shear-wave splitting measurements it mainly matters how the radial component looks relative to the transverse component. This is why shear-wave splitting studies do not usually compare waveform shapes of different SmKS phases on the same seismogram (e.g., Niu & Perez, 2004; Long & Lynner, 2015; Reiss et al., 2019; Asplet et al., 2020; Lutz et al., 2020). In Figure 4, only little energy arrives on the transverse component of the SKS beam (Figure 4a); accordingly, the particle motion is almost linear and the measurement would be classified as null. In contrast, both the SKKS and S3KS phases exhibit clear partitioning of energy to the transverse component (Figure 4b,c) with elliptical particle motions, indicating significant splitting. The estimated splitting parameters ($\phi$, $\delta t$) for these phases are (115°, 0.8 s) for SKKS and (119°, 0.9 s) for S3KS. The estimated splitting intensity for SKKS and S3KS is similar (0.6 and 0.8), while $SI$ is lower for SKS (0.2). This measurement is therefore an example of clearly discrepant SKS-SKKS-S3KS splitting, likely caused by the presence of lowermost mantle anisotropy, which is affecting the splitting of one or more phases. Specifically, the observation that the splitting intensity measured from SKS is different than for SKKS and S3KS (for which $SI$ is similar) can be explained if SKKS and S3KS sample similar lowermost mantle anisotropy, whereas the SKS travels through D″ in a region with different anisotropy (Figure 1a). Alternatively, all three phases may sample similar anisotropy in the lowermost mantle, and differences in splitting could be explained by the difference in incidence angle of these SmKS phases through the lowermost mantle (Figure 1a).

The measurements in Figure 4 demonstrate that splitting parameters can be retrieved from beamformed data for multiple SmKS phases for the same source-receiver configuration, and that they can be well-constrained with tight confidence intervals. To our knowledge, this is the first published splitting measurement for an S3KS phase. The measurement of robust SKS, SKKS and S3KS splitting parameters for beams constructed for the same single-station seismograms enables us to explore differential splitting for more than two phases, extending beyond the commonly used SKS-SKKS approach.

## 5 Averaging of seismic anisotropy contribution in beams

Here, we investigate how the shear-wave splitting signature that can be observed in individual single-station seismograms manifests in beams. While splitting will likely be primarily due to upper mantle anisotropy for most waves (e.g., Liu et al., 2014; Lutz et al., 2020), some arrivals may also be substantially influenced by seismic anisotropy in the deep mantle. For the purpose of this analysis, we investigate how the shear-wave splitting signature averages across subarray stations used in beams, without needing to distinguish explicitly between an upper and lowermost mantle anisotropy contribution. This also means that we can use the same analysis strategy for all waves, independent of potential upper and lowermost mantle contributions.

### 5.1 Real data observations

We focus on the full dataset shown in Figure 1a. For each event, we compare beam splitting parameters of SKS and SKKS phases to the average of the corresponding single-station splitting measurements ($\phi$, $\delta t$, $SI$; with a circular averaging approach used to average $\phi$ values). Our motivation for this comparison is to understand how the single-station splitting parameters, which themselves reflect seismic anisotropy integrated over a finite mantle volume, are averaged in a beamformed stack, particularly in regions which have laterally heterogeneous anisotropy.

We present the results for all events for both SKS and SKKS phases in Figure 5. For each subarray, represented by its central station, we present the splitting parameters as sticks, with their angle to the north indicating the fast polarization direction and their length proportional to the delay time. We show the results for all subarrays for which, in addition to well-constrained beam splitting, we obtained at least four (Figure 5a) and eight (Figure 5b) well-constrained single-station splitting measurements, respectively. Splitting parameters are defined as well-constrained if the 95% confidence intervals on $\phi$ are smaller than $\pm 20^\circ$ and smaller than $\pm 0.5$ s on $\delta t$. Figure 5 shows that the average of the single-station splitting parameters generally agrees well with the measured beam splitting. The minor differences that exist between beam and average single-station splitting will be analyzed in more detail below, with focus on splitting intensity measurements.

For smaller SNR data, the splitting intensity, $SI$ (Chevrot, 2000), can be a more robust measurement quantity than the traditional splitting parameters ($\phi$, $\delta t$) (see Mon-

teiller & Chevrot, 2011). Because beam splitting parameters approximately agree with the average single-station splitting of all seismograms that make up the beam in Figure 5, we next test whether this is also the case for $SI$. We analyze the $SI$ difference between beam and average single-station splitting for the same dataset, only considering beam or single-station $SI$ measurements whose 95% confidence intervals are smaller than $\pm 0.5$ (Figure 6, first column). We also show the standard deviations of the mean of the single-station $SI$ measurements (Figure 6, second column). Each panel represents the results for a different minimum number of well-constrained single-station $SI$ measurements per subarray (first row: $\geq 4$; second row: $\geq 8$; third row: $\geq 12$; fourth row: $\geq 16$). For a large majority of measurements, we find that the difference in average single-station and beam $SI$ is smaller than 0.3. For measurements for which the $SI$ difference is relatively large, the standard deviation tends to be large too, indicating non-uniform single-station splitting across the subarray. We find that in general, the greater the measurement number of well-constrained single-station splitting measurements that can be obtained for the subarray, the smaller the difference in $SI$ tends to become. As the number of well-constrained single-station measurements that can be obtained will depend largely on SNRs, these results also indicate that for higher SNRs, beam and average single-station splitting will be more similar. We note that the results presented so far do not indicate whether single-station or beam seismograms are more suitable to accurately characterize the anisotropy in cases in which they disagree; we will explore this point further below.

While it is apparent that, generally, the beam splitting parameters represent an average of the single-station splitting parameters, some deviations from this rule can be observed in Figures 5 and 6. To understand better the reasons for these deviations, we investigate how the difference in $SI$ between the single-station average and the beam splitting depends on several factors, including the standard deviation of the single-station $SI$ mean, the absolute value of the beam $SI$, the mean single-station $SI$ confidence interval, as well as the mean single-station and beam SNRs. We additionally demonstrate how SNRs are improved through beamforming. These results are shown in Figure 7, which illustrates linear fits through the measurements in each plot, for subarrays for which at 4 and at least 16 well-constrained single-station splitting measurements could be obtained, respectively. We do not imply that we necessarily expect linear relationships; rather, these fits enable us to see general trends despite the large number of measurements.

In Figure 7a, we first show the mean of the single-station $SI$ values as a function of the beam splitting intensity. The trend is linear with a slope of 0.80 ($\geq 4$ well-constrained single-station measurements) and 0.91 ($\geq 16$), respectively (close to 1), as expected from the results presented in Figures 5 and 6. However, mean single-station $SI$ values tend to be slightly lower than beam splitting intensities. In panel b of Figure 7, we show the mean size of the single-station 95% confidence intervals for $SI$ as a function of the size of the beam 95% confidence interval. As would be intuitively assumed, the larger the mean of the single-station confidence intervals is, the larger the confidence interval for the beam tends to be, although this can only explain part of the variation ($R^2 = 0.22$). In panels c-e, we show how the absolute difference between mean single-station $SI$ and beam $SI$ depends on (c) the standard deviation of the mean of the single-station $SI$ measurements; (d) the absolute value of the beam $SI$; and (e) the mean size of the single-station 95% confidence interval. While the $SI$ difference cannot be well explained by the quantities explored in (c) and (d), for subarrays for which $\geq 16$ single-station splitting measurements can be obtained, the $SI$ difference tends to larger for larger mean single-station 95% confidence intervals ($R^2 = 0.27$). In panel (f) we show the beam SNR as a function of the mean single-station SNR. The linear fits show slopes of 2.28 ($\geq 4$) and 3.93 ($\geq 16$), indicating that the beam SNR is on average more than twice as large than the mean single-station SNR. Panel (g) shows how the $SI$ difference depends on the mean SNR of the individual single-station $SI$ measurements. Panel (h) shows the same for the SNR of the of the beam. The $SI$ difference tends to be inversely proportional to the (mean) SNRs in panels g-h but the trends can only poorly explain the variation ($R^2 \leq 0.03$) when all data are considered together. A (seemingly) contradictory observation is that the $SI$ difference tends to be lower for cases in which $\geq 16$ well-constrained single-station splitting measurements can be obtained per subarray, considering that the number of well-constrained single-station measurements that can be obtained will be mainly influenced by single-station seismogram SNRs. However, in panels g-h, many more subarrays with lower mean single-station SNRs (1.5 to 5) are presented than with higher SNRs ($\geq$ 5), which may skew trends. We will therefore pay particular attention to the role of SNRs in the following when zooming in on a specific subset of the data.

Relatively large differences between average single-station and beam $SI$ values can be observed for a region of the Cascadia backarc known as the High Lava Plains (HLP) region (black box in Figure 6). We analyze these data in more detail to understand why

our assumption about how upper mantle anisotropy averages in beams is not fully accurate for this particular region, which has been shown to exhibit strong SKS splitting with generally uniform, nearly east-west fast directions and laterally variable delay times (Long et al., 2009; Mondal & Long, 2020). In this test, we take advantage of the dense station spacing provided by stations of the High Lava Plains seismic experiment (Long et al., 2009). First, we test whether the difference in $SI$ between the average of the single-stations and the beams is reduced by using a larger number of stations for the beams (Figure 8b-d). For this test, we run beams for this region while allowing a maximum number of 20 (b), 30 (c) or 40 (d) individual single seismic stations to be included in each beam (and thereby increasing the subarray's aperture). Figure 8 demonstrates that increasing the number of stations used for the beamforming does not lead to more similar average single-station and beam splitting, perhaps because increasing the station number also increases the subarray aperture.

For further analysis, we add the data from our HLP test to the plots shown panels a, b and g of Figure 7. These results are shown in Figure 8 e-g. We find that independent of how many stations are used to construct the beam, the mean single-station $SI$ tends to be substantially lower than the beam $SI$ (Figure 8e), while mean single-station $SI$ 95% confidence intervals are relatively large (f) and SNRs from the single-station seismograms are low (g). We speculate, therefore, that the relatively large difference between single-station and beam $SI$ values in the HLP region can perhaps be explained by the relatively poor data quality (and thus low SNRs) for the single-station seismograms obtained for the event used. To test this, we plot the data for mean single SNR values $>$ 5 or $<$ 5 separately (Figure 8h-j). We find that for SNRs $>$ 5, the mean single-station $SI$ values tend to agree very well with the beam $SI$ (linear fit with slope=0.94; Figure 8h). For SNRs $<$ 5, on the other hand, the mean single-station $SI$ values underestimate the magnitude of the beam $SI$ (linear fit with slope=0.78; Figure 8j). (We also confirm this result with a synthetic test, which is described in Section 5.2). Additionally, the mean single-station $SI$ 95% confidence interval and the $SI$ difference between beam and average single-station splitting are more strongly correlated with the beam $SI$ 95% confidence interval for SNRs $>$ 5 (Figure 8i-j,l-m).

To ensure that our interpretation of large $SI$ differences being due a high noise level affecting the single-station seismograms holds, we also construct beams for another event for the HLP region. For this other event, the differences in splitting intensity between

beam and average single-station splitting are generally lower (Supplementary Figure S1), indicating that the $SI$ differences for the HLP region can in fact be explained by the details of the data for the initially used event. The results of these tests suggest that for noisy data, $SI$ values may generally be underestimated, consistent with conclusions drawn by other studies (e.g., Hein et al., 2021). We will further discuss this finding below in Section 7.

### 5.2 Synthetic tests

Next, we conduct a series of tests using synthetic input models to refine our understanding of how beam splitting averages anisotropic structure across heterogeneous, anisotropic regions. We use AxiSEM3D to conduct both axisymmetric and fully 3D global wavefield simulations down to ∼5 s period, using PREM (Dziewonski & Anderson, 1981) as our radially symmetric background model. Our simulations include 1D attenuation (from PREM) and Earth's ellipticity. In our simulations, we place the source at (60°N, 150°W) and an we construct a synthetic array centered on (0°N, 30°E) with a station separation of 0.5° (see Figure 9). The only nonzero component of the source moment tensor is $M_{tt}$; while this is not a realistic seismic source, the moment tensor is only important for this study insofar as this leads to substantial initial source SV-energy and thus high amplitude SmKS phases in the synthetic seismograms.

We make use of the anisotropic module implemented into AxiSEM3D by Tesoniero et al. (2020), which allows the computation of synthetic seismograms for arbitrary seismic anisotropy. We conduct simulations for a set of simple models that include upper mantle anisotropy. As we focus here on how the anisotropic signature averages in beams, we could just as well carry out this test by considering lowermost mantle anisotropy, or both upper and lowermost mantle anisotropy. However, we choose to implement seismic anisotropy only in the upper mantle because such a scenario is very straightforward to understand. We implement lateral transitions of upper mantle anisotropy across the seismic array, similar to synthetic experiments carried out by Wolf et al. (2022b) for lowermost mantle anisotropy. We always incorporate a horizontally transversely anisotropic (HTI) elastic tensor into the upper mantle, replacing PREM velocity structure between 24 and 220 km depth. The anisotropy that we incorporate leads to a delay time of ∼1.0 s for SmKS phases at the receiver. To investigate how measurements of anisotropy in beams that spatially average across the array compare to single-station measurements, we con-

struct the following models of upper mantle anisotropy across the (sub-)array (see Figure 9):

1. Setup 1 (Figure 9b): Uniform anisotropy across the array. We implement three cases, with three different anisotropic fast directions, for which the angle between the backazimuth (that is, the initial wave polarization direction) and fast direction of the HTI anisotropy is 0° (case 1), 30° (case 2) and 60° (case 3), respectively.
2. Setup 2 (Figure 9c): We implement a transition between two anisotropic domains with different geometries. Again, we implement three cases, varying the angle between initial polarization of the wave (or, equivalently, the backazimuth) and the fast polarization direction of the anisotropy. The fast polarization directions that we implement for both anisotropic domains are orthogonal to each other, allowing us to evaluate the averaging of splitting across the array in a straightforward manner. This is because splitting due to layers of anisotropy with orthogonal fast directions should effectively cancel.

For the first benchmark setup, uniform upper mantle anisotropy is present across the array, as shown in the first row of Figure 10. For uniform anisotropy across the array (top panel in Figure 10), beam splitting agrees very well with the average single-station splitting. For the second setup, we place a transition between two contrasting (orthogonal) anisotropic domains in the upper mantle beneath the array (Figure 10, middle row). We expect that measurements that sample equally across both domains should be null, as the effects of splitting cancel. We find that while the single-station seismograms are clearly split for the stations that are not very close to the transition between both anisotropic domains (middle station row), the beam splitting is null, in agreement with the idea that beam splitting represents the average of the single-station splitting. The lower row of Figure 10 shows results for which we only perform beamforming for a subset of stations from the array. In this series of tests, we progressively remove one station row from one of the anisotropic domains, such that the other domain dominates the overall beam splitting (left column). This becomes even clearer when excluding additional station rows from the beamforming (middle column). When we only apply the beamforming to stations above one of the anisotropic domains, the results agree with those from setup 1 that includes uniform upper mantle anisotropy (lower row, right column).

Example synthetic single-station and beam waveforms from this experiment are shown in Supplementary Figure S2.

In order to understand further how noise affects both the single-station and the beam measurements, we also conduct a test for which we systematically add Gaussian noise to the single-station synthetic data from setup 1 and case 2 and then conduct the beamforming (Figure 11). We find that the beam splitting intensity estimate is relatively independent of the single-station noise level, although the 95% confidence interval tends to increase as noise is added. The average single-station splitting intensity, on the other hand, decreases as noise is added, which is in agreement with the real-data results from the HLP region (Section 5.1) and is also in agreement with findings from previous papers (Monteiller & Chevrot, 2011; Hein et al., 2021). This implies that beam splitting parameters are more reliable at characterizing the anisotropy than single-station splitting measurements if noise levels are high. Additionally, and importantly, Figure 11e demonstrates that even if no well-constrained single-station measurement can be obtained, beam splitting can still be robust and reliable for the array. As higher noise levels are added, the beam approach breaks down for average single station SNRs $< 1.3$. This indicates that the beamforming approach is unlikely to be effective at determining shear-wave splitting measurements if the contributing single station seismograms have a mean SNR $< 1.3$. This is a substantial advantage compared to single-station $SI$ measurements whose reliability starts to break down at larger SNRs (SNRs $< 2$; see Supplementary Figure S3).

## 6 Potential applications of SmKS beam splitting

We have investigated in Section 5.2 how the splitting signature from single-station seismograms averages in beams and shown that the splitting intensity of the beam will approximately equal the arithmetic mean of the single-station splitting intensities. Furthermore, we have shown that beamforming increases SNR and leads to more robust and reliable splitting estimates for noisy data. This observation suggests that splitting analysis of beamformed data can help reliably resolve mantle anisotropy. It is commonly assumed that splitting contribution of upper mantle anisotropy dominates over the influence of deep mantle anisotropy for SKS and SKKS phases (e.g., Niu & Perez, 2004; Liu et al., 2014; Walpole et al., 2014). Under this assumption, which is commonly made in traditional SmKS splitting studies, beam splitting measurements can be used to characterize seismic anisotropy in the upper mantle. However, there is a tradeoff between higher

SNRs and the loss of spatial resolution. Beam splitting can be interpreted as the average upper mantle splitting across the (sub-)array. Our tests have shown that this will generally be a more reliable measure of the overall splitting contribution than averaging single-station splitting measurements if noise levels are high (Figure 11). However, this comes at a cost: the beam splitting averages spatially, so small-scale variability in upper mantle anisotropy cannot be resolved.

For some applications, it may not be a disadvantage that the contribution of upper mantle anisotropy is averaged laterally. For instance, measurements of differential SKS-SKKS splitting are typically interpreted as evidence for the presence of deep mantle anisotropy (e.g., Tesoniero et al., 2020; Asplet et al., 2020) and are often made difficult by low SNRs and the challenge of identifying high-quality SKS and SKKS phases on the individual seismograms. While the use of beamformed data will also lead to a loss of spatial resolution of lowermost mantle anisotropy, the amount of scatter for single-seismogram differential SKS-SKKS splitting measurements (e.g., due to noise) usually does not allow the analysis of small-scale deep mantle anisotropy patterns in any case (e.g., Reiss et al., 2019). We suggest, therefore, that beamform approaches have the potential to significantly improve studies of lowermost mantle anisotropy via SKS-SKKS differential splitting measurements.

We illustrate these points by showing a proof-of-concept example for the SKS-SKKS differential splitting technique, applied to beamformed data. We choose two events (2009-10-07, 2011-09-05) whose raypaths sample the lowermost mantle beneath the northeastern Pacific Ocean, because for this region, particularly pronounced SKS-SKKS differential splitting has been found in previous studies (Long, 2009; Asplet et al., 2020; Wolf & Long, 2022).

We measure SKS-SKKS splitting intensity discrepancies from beamformed data (Figure 12a) as well as from the single-station data that is used to create the beams (Figure 12b). The black, dashed ellipse in Figure 12 indicates the region for which discrepant SKS-SKKS splitting has been previously observed by Wolf and Long (2022). Consistent with these previous results, we find that in this region, generally discrepant SKS-SKKS splitting can be observed, for both beam and single-station splitting measurements. A little further to the east and west, splitting tends to be nondiscrepant, which is also consistent with the observations of Wolf and Long (2022). Another swath of raypaths sam-

ples the lowermost mantle beneath southern Canada, which is a region for which, to our knowledge, SKS-SKKS splitting discrepancies have not been analyzed in the past. Both the beam and single-station splitting measurements tend to be nondiscrepant for this raypath geometry.

While the general patterns of SKS-SKKS splitting intensity discrepancies are similar for beam and single-station SKS-SKKS splitting discrepancy measurements, the measurements from the beamformed data show much less scatter (Figure 12). In the single-station measurements, we often observe different behavior for directly adjacent raypaths, which is likely due to scatter caused by noise and not by lowermost mantle structure, suggesting that the beam measurements are more reliable. Figure 12 shows all well-constrained measurements (95% confidence intervals $< \pm 0.5$) that could be obtained from this particular dataset for beams and single stations. For the single-station data, we obtain approximately three times more usable discrepancy measurements than from the beams. However, by construction of the beams, we have approximately 15 times more single-station seismograms available for measurements than beams (because 10-20 seismograms are used to create a beam), meaning that roughly five times more data contribute to our beam splitting discrepancy analysis overall.

## 7 Discussion and conclusion

For the interpretation of shear-wave splitting measurements from beamformed data, it is important to understand how the splitting signature from the single seismograms contributes to the beam's splitting signature. To explore this, we applied the beam splitting technique to real data for subarrays across USArray and compared our results to single-station splitting. We also carried out synthetic tests using simple but heterogeneous upper mantle anisotropy models. These results indicate that beam splitting generally agrees with the average of the single-station splitting for those seismograms that contribute to the beam. This average can be expressed either in terms of the splitting parameters ($\phi$, $\delta t$) or $SI$.

We have shown that shear-wave splitting measurements can be performed using beamformed SmKS data, which has the advantage of higher SNRs compared to single-station seismograms. This enables us to measure shear-wave splitting from phases that are not usually used for this purpose; for example, S3KS phases (Figure 3). The inclu-

sion of additional seismic phases in shear-wave splitting studies makes it possible to use earthquakes from a large distance range and to exploit less commonly used ray geometries. This leads to new possibilities for the characterization of seismic anisotropy in Earth's mantle and may be particularly powerful for studies of lowermost mantle anisotropy, which are often hampered by limited ray coverage and by difficulties in isolating the lowermost mantle contribution. The beam approach can, in principle, be used for any seismic phase. We are currently exploring the application of beamformed data in lowermost mantle splitting studies using phases other than SmKS, such as $S_{diff}$ and ScS. We are also working to routinely incorporate S3KS phases into studies of lowermost mantle anisotropy using SmKS splitting discrepancies.

Our real-data analysis does not show evidence that laterally changing anisotropy across a subarray affects how accurately the beam splitting reflects an average of the single-station splitting parameters (Figure 6). Rather, simple synthetic modeling suggests that such averaging works remarkably well if a transition between two anisotropic domains is incorporated across the (sub-)array (Figure 10). Similarly, 3D effects to the waveforms caused small structures close to the receivers, potentially influencing splitting measurements, likely influence beams less than single-station measurements. Rather, effects of such small-scale scattering will be laterally averaged in beams, such that beam splitting measurements will be largely unaffected.

While it is generally true that beam splitting agrees with average single-station splitting, we find that if single-seismogram SNRs are low, the beam $SI$ values tend to be larger than the average single-station $SI$. Our results indicate that this is due to the fact that high noise leads to an underestimate of $SI$ for the single-station seismograms, meaning that the beam $SI$ measurement will be a more accurate reflection of the splitting signal than the single-station measurements (Figure 11). This implies that splitting intensity, measured from single-station data, provides a lower bound for the actual value, which should be considered in their geologic interpretation (see also Monteiller & Chevrot, 2011; Hein et al., 2021). We suggest that if $SI$ values are used to identify the strength of seismic anisotropy, it should generally be ensured that SNRs are sufficiently large. Similarly, if we compare $SI$ values from different seismic phases (for example, in the context of SKS-SKKS differential splitting), care must be taken to ensure that the noise level affecting both phases is similar. In any case, however, increasing SNR levels via beamforming is a promising approach.

The beamformed SmKS splitting technique opens avenues for novel shear-wave splitting analyses. We can also use traditional splitting techniques for beamformed data. This approach yields larger SNRs and more robust measurements for beams, although it comes at the cost of lateral averaging of the anisotropic signature. The measurement of beam splitting may be helpful for the characterization of upper mantle anisotropy, especially if single-station SNRs are low, although this approach will obscure any lateral variability on length scales smaller than the subarrays used to construct the beams.

Beamformed data will be particularly helpful to resolve lowermost mantle anisotropy. The anisotropic signature associated with lowermost mantle anisotropy is often compromised by the upper mantle anisotropy contribution (e.g., Wolf et al., 2022a). Using beamformed data, we can select (sub-)arrays such that the upper mantle contribution to beam splitting is weak (e.g., by stacking data across regions with weak or laterally variable anisotropy). As an example, we measure SKS-SKKS differential splitting across USArray stations in the western US. The results obtained from beams are substantially less scattered than those from the single-station seismograms, likely because the stacking process naturally removes noise. We suggest that SKS-SKKS differential splitting measurements from beams are more reliable than from single-station seismograms. Future work will include applying this analysis strategy to study SmKS splitting discrepancies on a global scale using beamformed data.

To summarize, we have demonstrated that the application of shear-wave splitting on beamformed data and that beams average the single-station splitting signature across the (sub-)array. Due to increased SNRs, beamforming leads to better constrained shear-wave splitting parameters than single-station seismograms. Therefore, beamforming allows the ability to measure splitting parameters from phases that are usually too low quality for individual seismograms to be useful for splitting analyses. As a result, we can use traditional splitting techniques for beamformed data. Therefore, the measurement of shear-wave splitting from beamformed data has potential for improving estimates of both upper and, especially, lowermost mantle anisotropy.

## Data and software availability

All USArray data (IRIS Transportable Array, 2003) and data from the High Lava Plains experiment were downloaded through IRIS (`https://service.iris.edu/`). The

synthetic seismograms for this study were computed using AxiSEM3D which is publicly available at `https://github.com/AxiSEMunity`.

**Acknowledgments**

This work was funded by Yale University and by the U.S. National Science Foundation via grant No. EAR-2027181 to DAF, EAR-2026917 to MDL, EAR-1853911 to EG, EAR-1855206 to NC and EAR-2026931 to EB.

We thank the Yale Center for Research Computing for providing the necessary research computing infrastructure for this study. The Generic Mapping Tools (Wessel & Smith, 1998), ObsPy (Beyreuther et al., 2010), MSAT (Walker & Wookey, 2012), SplitRacer (Reiss & Rümpker, 2017), and AxiSEM3D (Leng et al., 2016, 2019) were used in this research.

## Figures

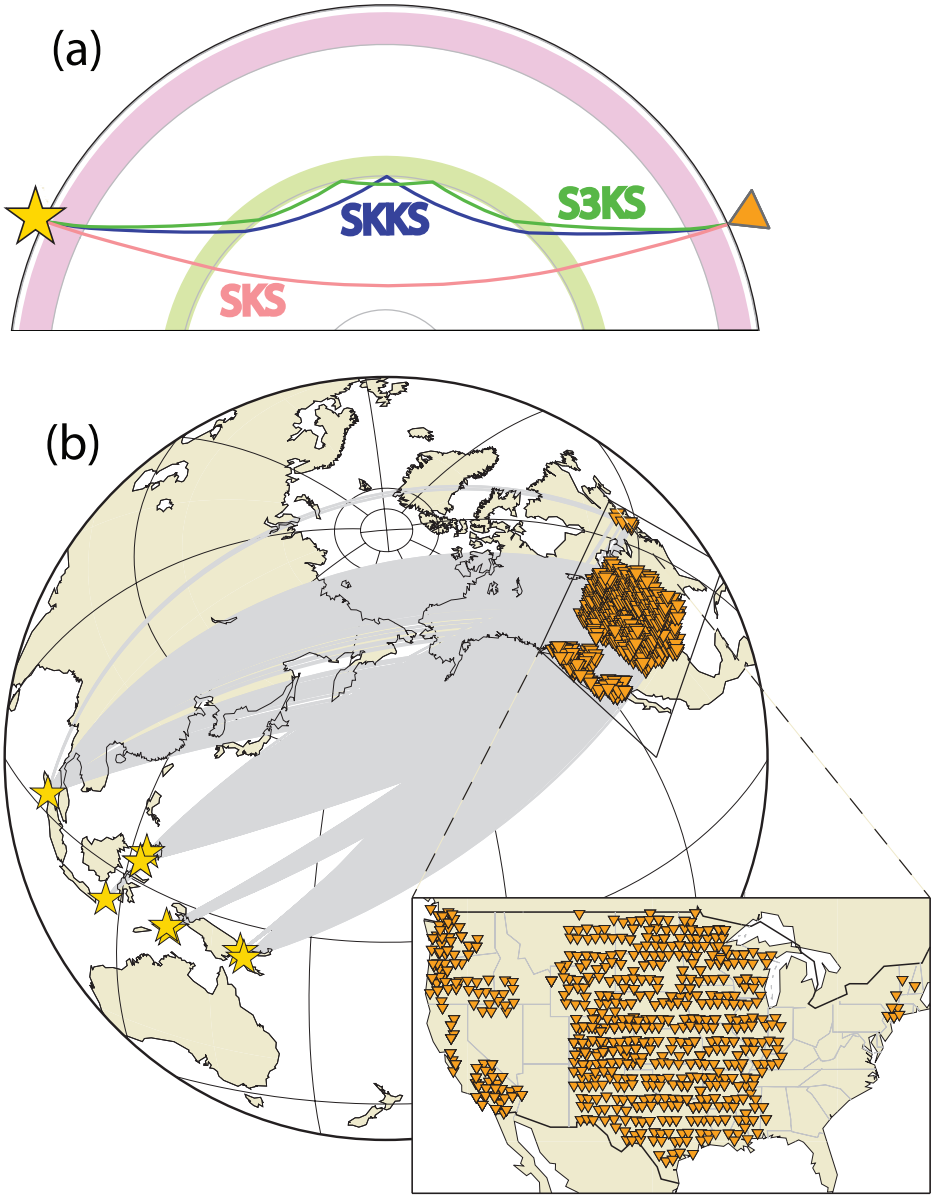


**Figure 1.** (a) SKS, SKKS and S3KS raypaths between source (yellow star) and receiver (orange triangle), shown in a cross-section for a source-receiver distance of 131°. Anisotropy can be found in the upper (pink) and lowermost (light green) mantle while the mid-mantle (white) is largely isotropic. (b) Source-subarray configuration used in this study. Sources are represented as yellow stars, central stations of subarrays as orange triangles, and raypaths from sources to subarrays (represented as central stations) as solid gray lines. A zoom-in presents the subarray coverage across the United States.

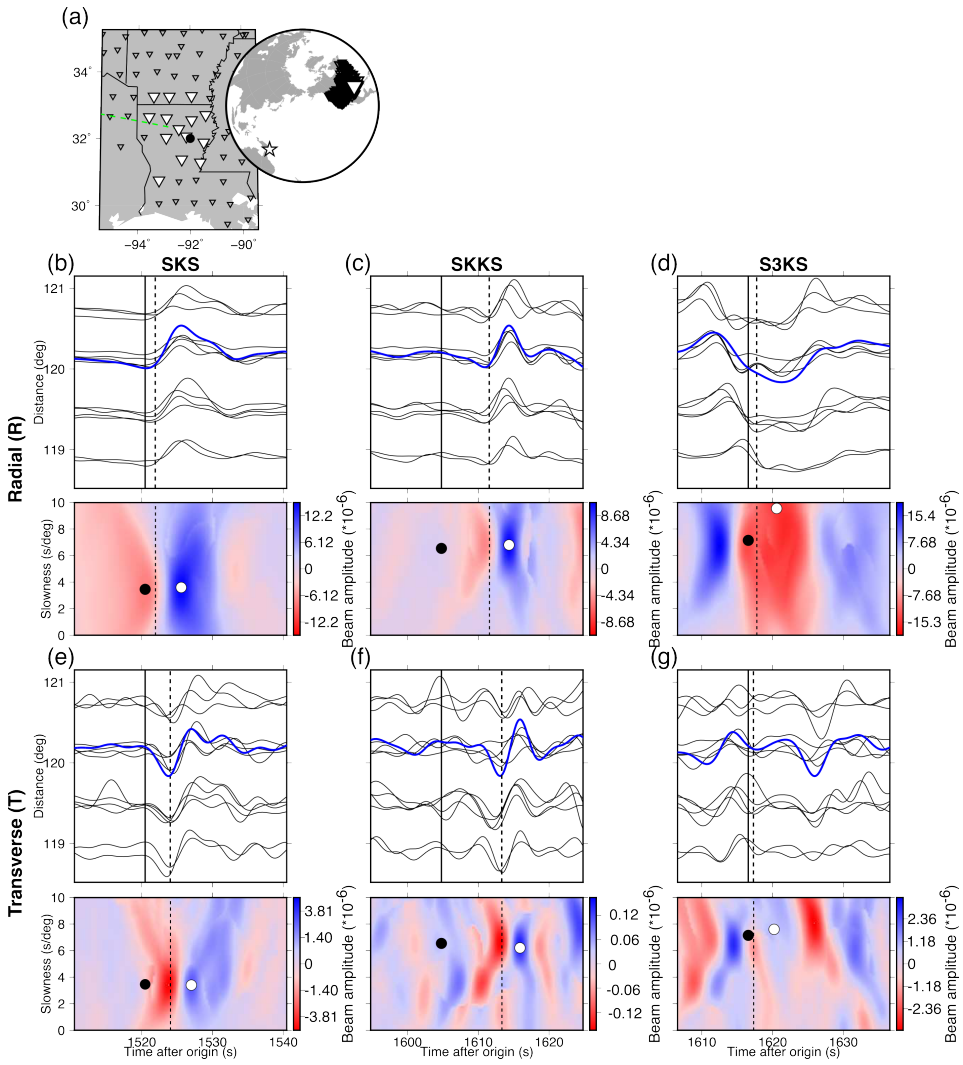


**Figure 2.** Illustration of the beamforming approach for an event that occurred on 2011/12/14 (Supplementary Table S1). (a) Stations are represented as triangles and plotted in white if belonging to the selected subarray. The subarray is located in the Southern US (see inset) and its center (black dot) is in Louisiana. Radial (b-d) and transverse (e-g) traces and vespagrams for SKS, SKKS, and S3KS phases recorded at the 13 USArray stations. Individual traces, normalized to the maximum amplitude across all traces, are aligned on (b and e) SKS, (c and f) SKKS, and (d and g) S3KS. The vespagram figures show beam amplitude (times $10^6$) as a function of slowness (y-axis) and time (x-axis). The PREM predicted arrival time and slowness of each phase are marked by the solid black vertical line and black circle, respectively, and the selected arrival time and slowness, for which the beam amplitude is maximum of all those tested, are marked by the dashed black vertical line and white circle respectively. The blue trace shows the beam constructed using the slowness marked by the white circle.

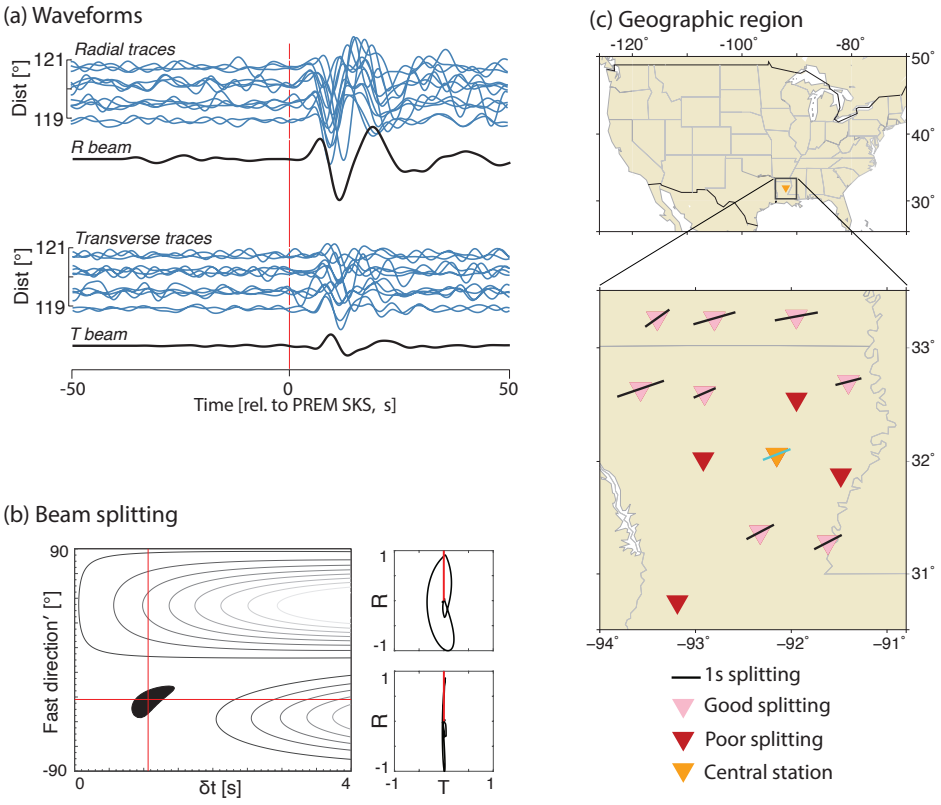


**Figure 3.** Representation of the splitting procedure used in this study for a subarray with central station 242A and an event that occurred on 2011/12/14 (Supplementary Table S1, Figure 2), demonstrated using the SKS phase. (a) Single-station (blue lines) radial (upper row) and transverse component seismograms (lower row) as a function of distance and corresponding beam traces (black). Single seismograms are aligned with respect to the SKS arrival time predicted by PREM (Dziewonski & Anderson, 1981), which is shown as a red line. (b) SplitRacer (Reiss & Rümpker, 2017) representation of the splitting measurements from the beam trace. Left side: Energy map in $\phi'$-$\delta t$ plane, with the 95% confidence interval of the splitting parameters shown in black and the best-fitting splitting parameters shown with red lines. $\phi'$ is calculated in a ray-attached coordinate frame, meaning that the traditional fast direction $\phi$ (in a station centered coordinate frame, measured from geographic north) and $\phi'$ are identical if the radial component is aligned with the north direction (see Section 3.2). Right side: Particle motions (black solid line) before (top row) and after (bottom row) correcting for splitting. The red line shows in the backazimuthal direction. (c) Top row: Location of the subarray, represented by its central station (yellow triangle). Bottom row: Zoom-in to all stations of the subarray (see legend). Single-station splitting parameters ($\phi$, $\delta t$) are shown as black sticks at the location of the station. The overall beam splitting is represented by the light blue stick and agrees well with the measured single-station splitting.

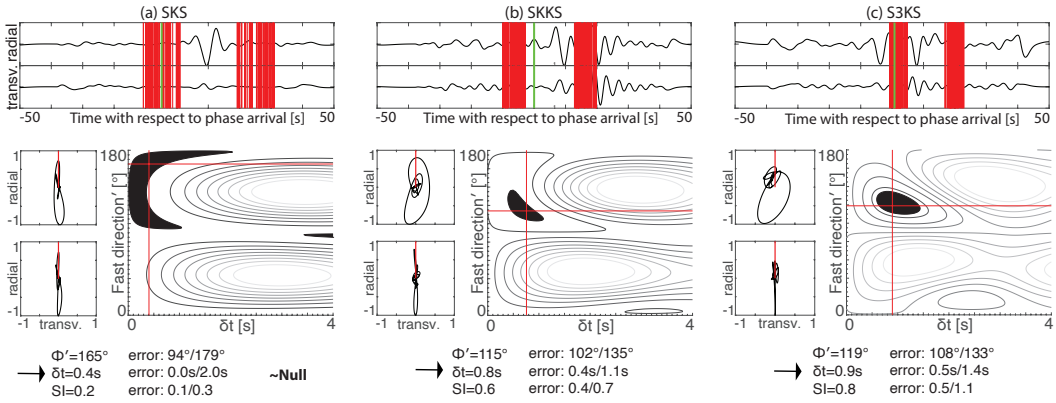


**Figure 4.** Splitting diagnostic plots from SplitRacer (Reiss & Rümpker, 2017) for the beam-formed waveforms from an event that occurred on 2010/07/29 (Supplementary Table S1) for a subarray in South Dakota, with a source-subarray distance of approximately 116°. (a) Top row shows the waveforms of the SKS stack (radial, top trace; transverse, bottom trace) as blue solid line, the predicted SKS arrival as a green line, and the start/end of the 50 randomly chosen measurement time windows with red lines. The upper diagram to the left shows the particle motion for the original stack (black line), the lower diagrams for the waveforms that were corrected for splitting. The red lines in the diagrams indicate the backazimuthal direction. To the right, the best fitting splitting parameters are shown in the $\phi'-\delta t$-plane, with black color indicating the 95% confidence region. The stacked SKS waveforms are only slightly split and would be characterized as a null measurement, with $SI < 0.3$. Best-fitting splitting parameters ($\phi$, $\delta t$, $SI$) are shown at the bottom. (b) Same representation as in panel (a), but for the SKKS phase. The SKKS phase is clearly split. (c) Same representation as in panel (a), but for the S3KS phase. The S3KS phase is clearly split, with similar splitting parameters as SKKS.

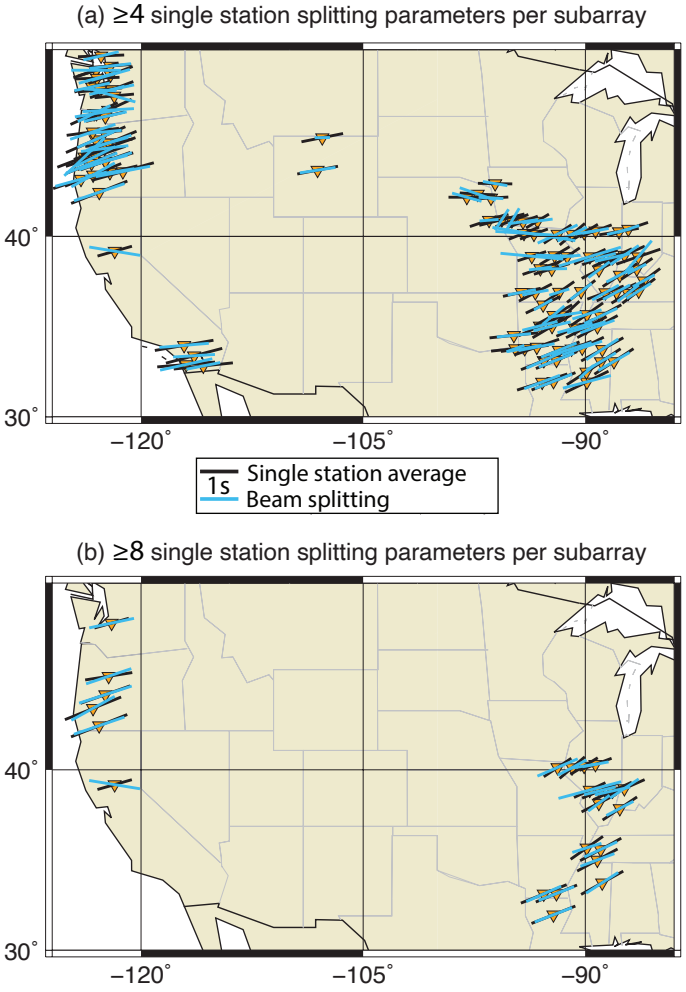


**Figure 5.** Comparison of average single-station splitting parameters ($\phi$, $\delta t$) for individual event-subarray combinations with the corresponding beam splitting for all data analyzed this study. This figure includes results for SKS and SKKS phases. While, in principle, SKS and SKKS splitting parameters could both be shown for a single station and plot on top of each other, this is not what practically happens. (a) Splitting parameters ($\phi$, $\delta t$) are shown as sticks, representing fast polarization directions (angle to the north) and delay time (proportional to the length, see legend). Sticks are plotted at the location of the central station of the subarray (yellow triangle) and colored either black (single-station average) or light blue (beam splitting). Single-station averages of the splitting parameters ($\phi$, $\delta t$) approximately agree with the beam splitting parameters. For this panel those subarrays are shown for which at least 4 well-constrained single-station splitting measurements could be obtained. (b) Same as panel a, but including subarrays for which at least 8 well-constrained single-station splitting measurements could be obtained.

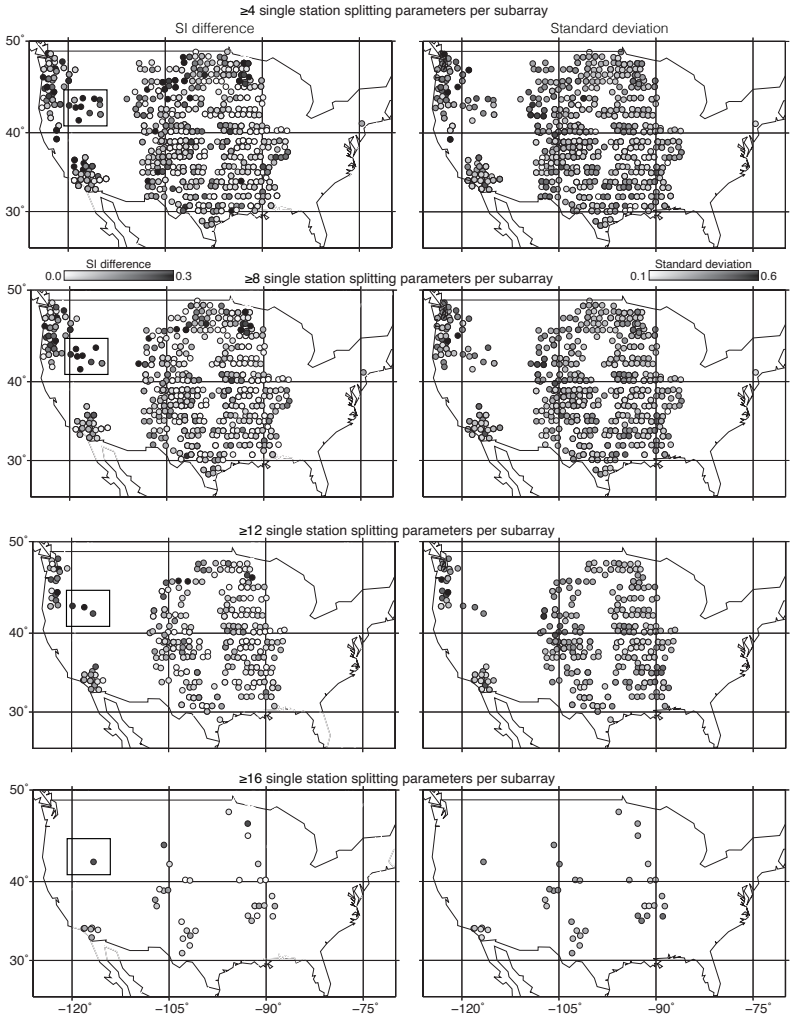


**Figure 6.** *SI* differences for (for SKS and SKKS phases, and all events) between the average of the single-station measurements for a subarray and the corresponding beam (first column) as well as standard deviations of the single-station mean splitting intensity (second column). First row: The absolute value of the splitting intensity difference and the standard deviation are plotted as a gray circles at the central station location of the subarray. The gray color scale indicates the magnitude of the difference (see legend). In this row all subarrays are included for which at least 4 well-constrained single-station splitting intensity measurements could be obtained. The High Lava Plains regions, for which *SI* difference values are relatively large, is marked by the black rectangle. Second row: Same as panel a for at least 8 well-constrained single-station splitting intensity measurements; third row: at least 12 well-constrained measurements; and fourth row: at least 16 well-constrained measurements. The *SI* difference and standard deviation tend to decrease the more single-station measurements are be obtained for a subarray.

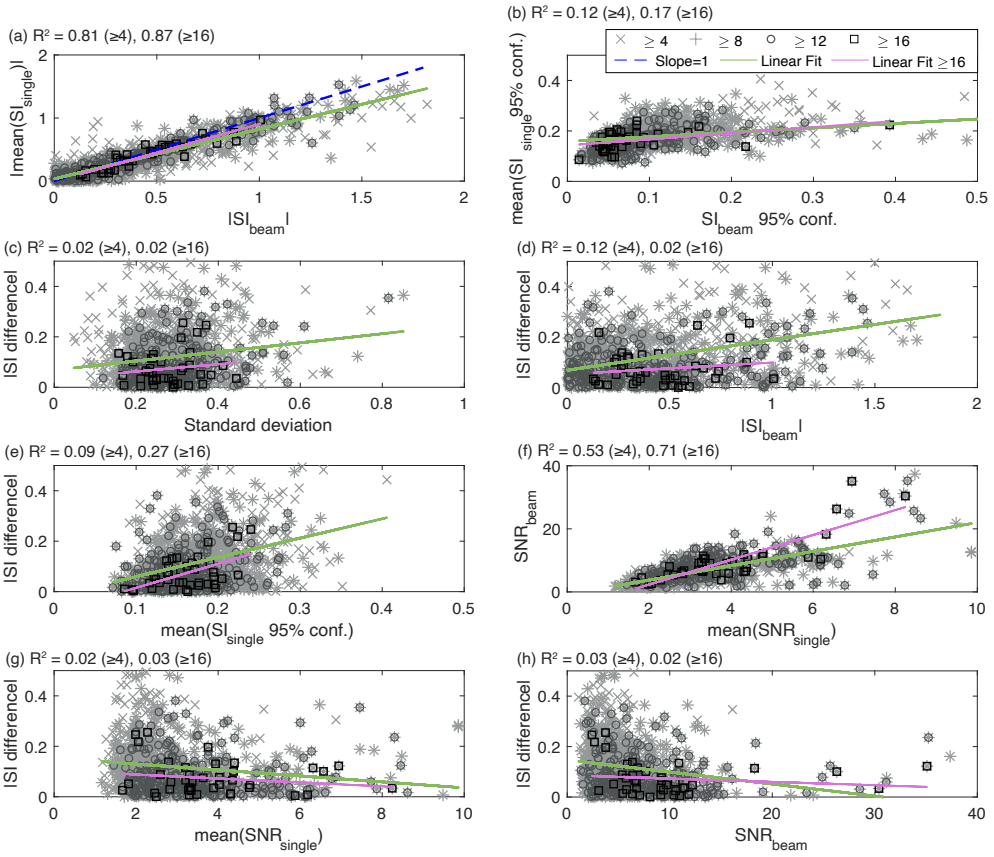


**Figure 7.** Dependence of beam and average single-station splitting intensities (and uncertainties), as well as their difference, on various factors. Different symbols are plotted for subarrays for which more than 4, 8, 12 and 16 well-constrained single-station $SI$ measurements could be obtained (see legend). Green ($\geq 4$ single-station measurements) and violet ($\geq 16$) lines are fitted into the measurement values to make trends visible. (a) Mean single-station $SI$ plotted against beam $SI$. A linear trend with a slope of 0.80 ($\geq 4$) or, respectively, 0.91 $\sim$1 ($\geq 16$) can be observed. (b) Mean size of the 95% confidence interval for the single-station measurements plotted against the confidence interval size of the beam. (c) Absolute value of the difference in $SI$ between the single-station average for a subarray and the corresponding beam splitting intensity, dependent on the standard deviation of the mean of the single-station $SI$ measurements. (d-e) $SI$ difference plotted against absolute value of the beam splitting intensity (d) and mean size of the single-station 95% confidence interval (e). (f) Beam SNR as a function of the mean single-station SNR. The linear slopes are 2.3 ($\geq 4$) and 3.9 ($\geq 16$) (g,h) $SI$ difference dependent on average single-station SNR and beam SNR.

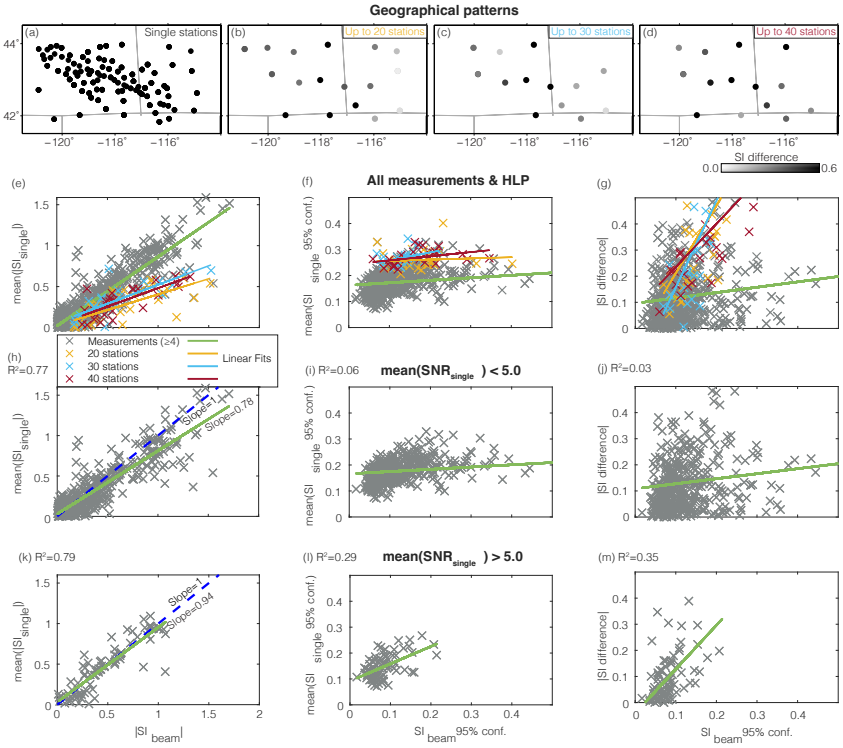


**Figure 8.** Detailed Investigation of HLP measurements for an event that occurred 2007/12/15 (Supplementary Table S1) and investigation of the influence of single-station SNRs for all events. (a) Individual stations used for beamforming. (b-d) *SI* differences between the average of the single-station measurements for a subarray and the corresponding beam. Similar plotting conventions as in Figure 6 (see legend). In each panel a maximum number of 20 (b), 30 (c) or 40 (d) stations is included in the beam. For every beam the total number stations included equals the maximum number or is slightly lower. The *SI* difference does not generally decrease if more stations are included in the beamforming. (e-g) Similar plotting conventions as in Figure 7 with linear fits represented as colored lines (see legend). Gray markers are as in Figure 7 for $\geq$4 well-constrained single-station measurements, while yellow (maximum 20 stations), blue (30) and red (40) markers correspond to the different station numbers of the HLP dataset. For the HLP region, for this particular event, the beam splitting intensity tends to be larger than the average of the single-stations (e), single-station 95% confidence intervals are relatively large (f) and SNRs are relatively low (g). (h-m) Similar to Figure 7, with measurements seperated according to SNR with SNR<5 (h-j) and >5 (k-m). For lower single-station SNRs (<5), the beam splitting intensity tends to be larger than the average of the single-station seismograms (linear fit of 0.79), while for larger SNRs (>5) both values tend to be similar (linear fit of 0.95).

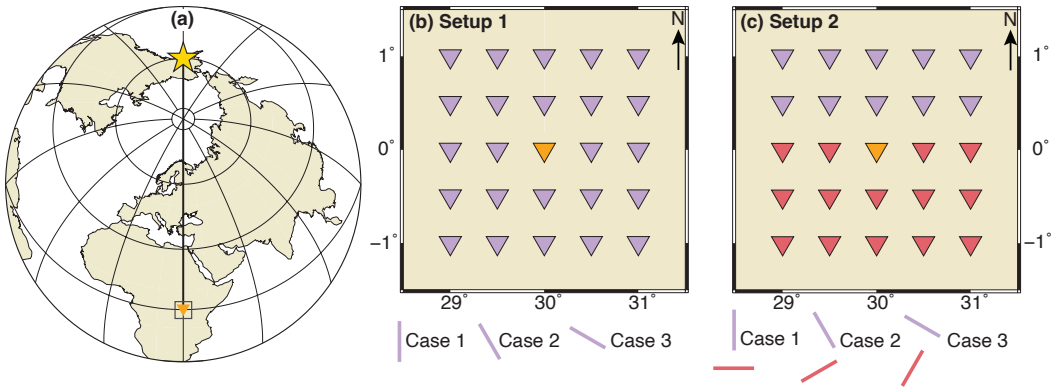


**Figure 9.** Model configuration for synthetic simulations that include HTI anisotropy in the upper mantle. (a) The raypath between source (yellow star) and central station of the array (yellow triangle) is shown as a black line. (b) Setup 1, for which we incorporate uniform anisotropy across the array. We calculate synthetic seismograms for 25 stations (violet triangles; central station: yellow triangle). Bottom: Sticks representing fast polarization directions (angle to the north) and delay times (proportional to the length) for three different rotations of the HTI elastic tensor. Strength of anisotropy is chosen such that delay times are always ∼1.0 s. (c) Setup 2, for which we incorporate a transition between two anisotropic domains. Stations above the first anisotropic domain are colored violet and stations above the second anisotropic domain are shown as light red triangles. The corresponding fast splitting directions are shown as sticks at the bottom as in panel b.

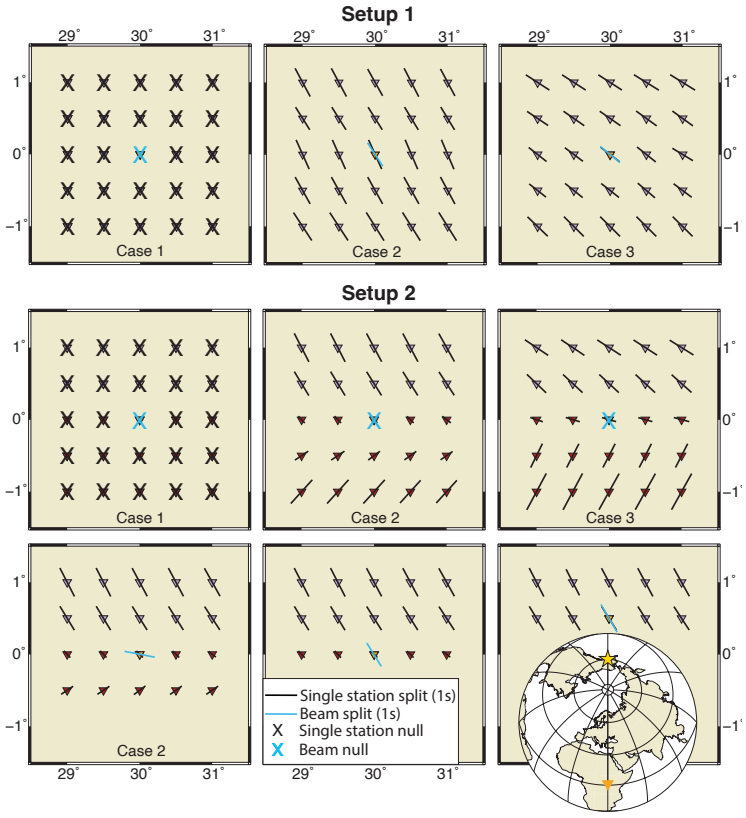


**Figure 10.** Shear-wave splitting results from beamformed SKS phases for the model configurations presented in Figure 9. Splitting parameters are represented as black bars (split) and Xs (null) for single stations, and in light blue for the resulting beam (see legend). Upper row: Results for setup 1 and cases 1, 2 and 3. The difference between these cases is the fast anisotropy direction of the HTI anisotropy incorporated into the upper mantle. For case 1, the backazimuth is in the direction of the fast polarization direction, leading to null splitting; for cases 2 and 3 splitting of the waveforms is evident and the beam splitting matches the individual station splitting well. Middle and lower row: Results for setup 2 and cases 1, 2 and 3. A lateral transition of anisotropy is implemented into the upper mantle, such that the fast polarization directions of the domains are orthogonal to each other (see Figure 9), with the transition between the anisotropic domains is in the middle of the array, the resulting beam splitting is null (middle row) as expected. In the lower row, we show beam averaging with different subarrays for setup 2, case 2, such that rows of stations are progressively removed from the beam averaging. As expected, when more stations are affected by one type of receiver side anisotropy than the other, the resulting splitting is approximately an average weighted by the number of stations influenced by each anisotropic domain. Waveforms for case 2 of setups 1 and 2 are shown in Supplementary Figure S2.

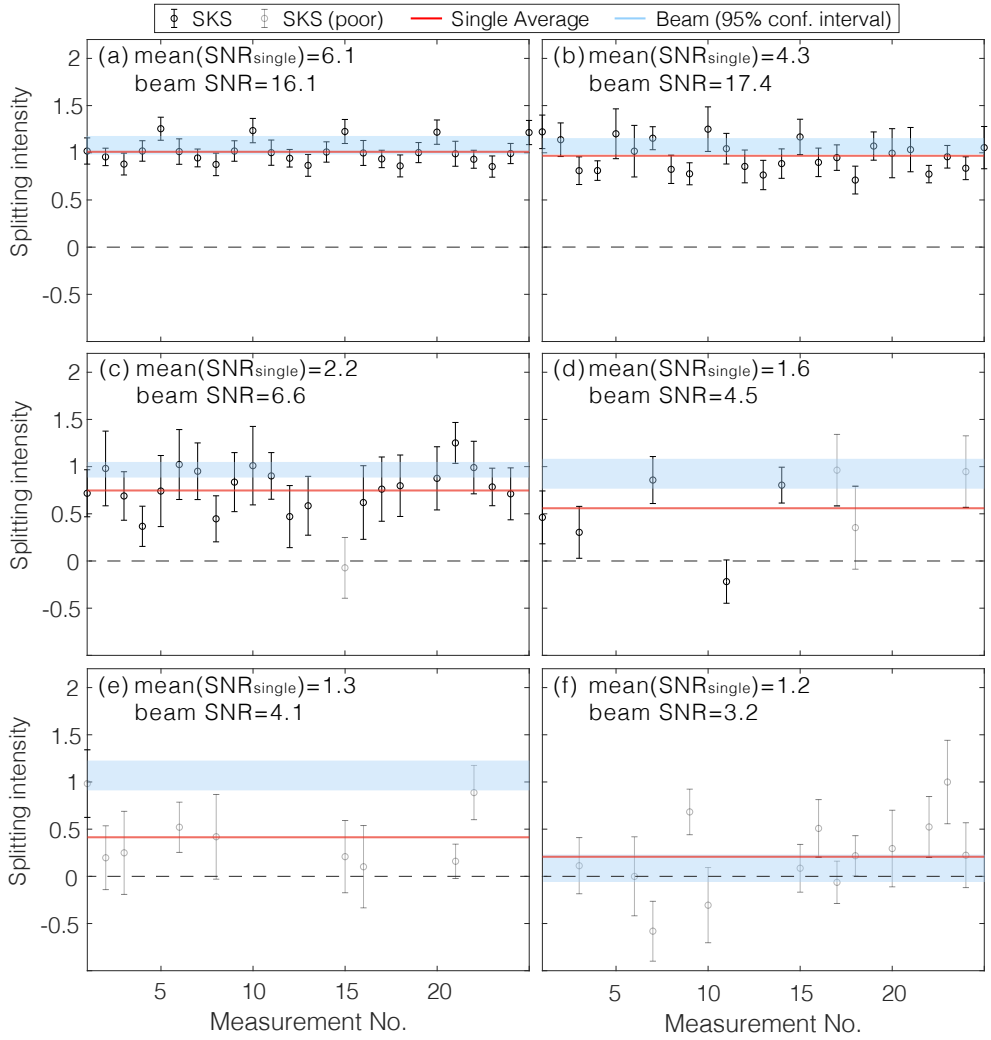


**Figure 11.** Behavior of single-station and beam splitting intensities for different noise levels of the single-station seismograms for for setup 1, case 2 (Figure 9). The noise level is increased from panel (a) to (f), with SNR values shown at top. Single-station (black markers with errorbars; indicating 95% confidence intervals) and beam (light blue region) splitting intensities are measured using SplitRacer (Reiss & Rümpker, 2017). The mean single station *SI* is shown as a solid red line. We only include measurements for which the 95% confidence intervals are smaller than ±0.5, and plot measurements that would be visually defined as poor in light gray (see legend).

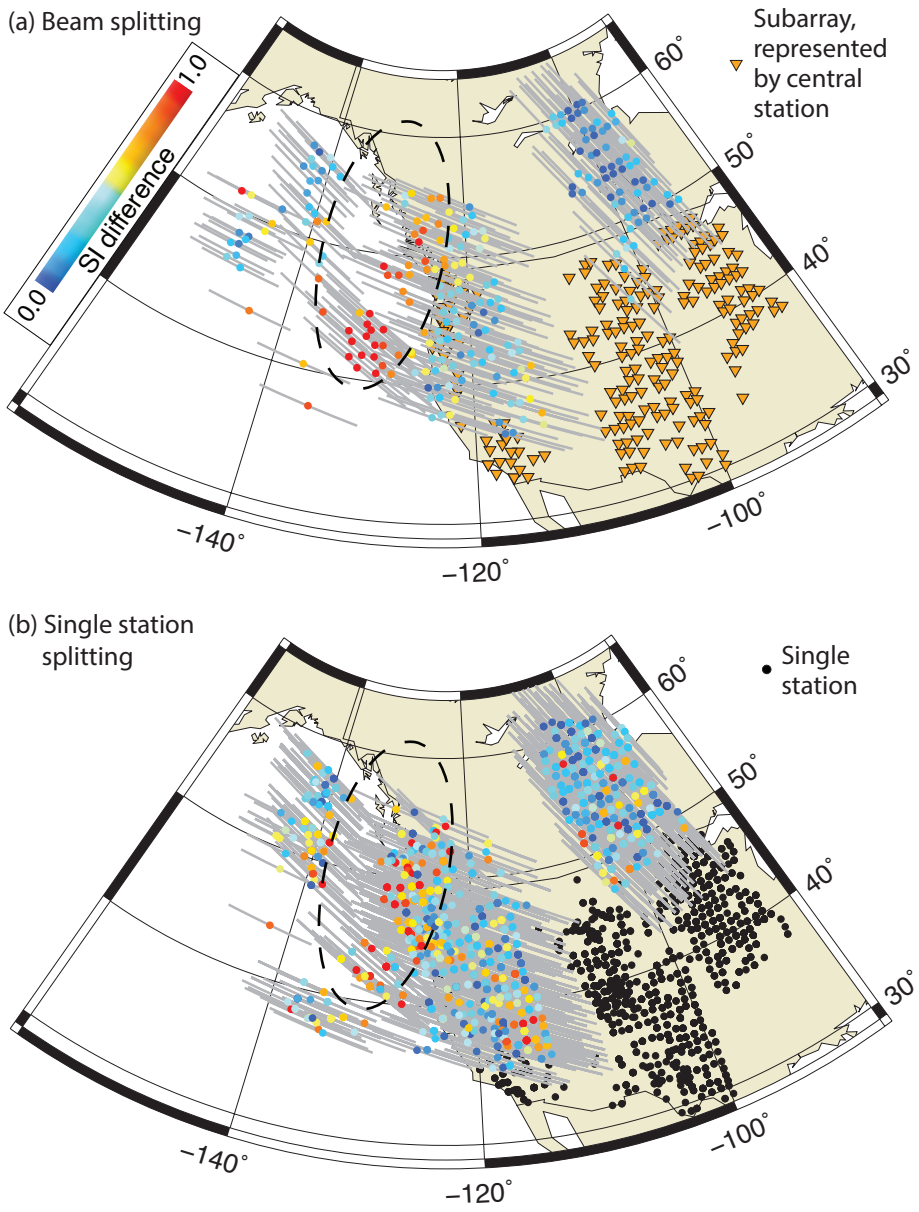


**Figure 12.** SKS and SKKS splitting intensity discrepancies for two example events (from 2009/10/07 and 2011/09/05, see Table S1), measured from (a) beamformed data and (b) single-station seismograms. The black dashed line indicates the region for which SKS-SKKS differential splitting was detected by Wolf and Long (2022). Colored circles represent the magnitude of the splitting intensity difference between SKS and SKKS phases (see legend) and are plotted in the middle of a gray line that connects the pierce point of SKKS 250 km above the CMB and the pierce point of SKS at the CMB. (a) Shows measurements for beamformed data with subarray central stations shown as yellow triangles. (b) Similar to panel a, but for single-station seismograms. Stations are plotted as black circles; plotting conventions are otherwise identical to panel a.

## References


Asplet, J., Wookey, J., & Kendall, M. (2020). A potential post-perovskite province in D″ beneath the Eastern Pacific: evidence from new analysis of discrepant SKS–SKKS shear-wave splitting. *Geophysical Journal International*, *221*, 2075–2090. Retrieved from https://doi.org/10.1093/gji/ggaa114

Barruol, G., Wuestefeld, A., & Bokelmann, G. (2009). SKS-Splitting-database. *Université de Montpellier, Laboratoire Géosciences*. Retrieved from https://doi.org/10.18715/sks_splitting_database

Becker, T. W., & Lebedev, S. (2021). Dynamics of the upper mantle in light of seismic anisotropy. In *Mantle Convection and Surface Expressions* (pp. 257–282). American Geophysical Union (AGU). Retrieved from https://doi.org/10.1002/9781119528609.ch10

Bercovici, D., & Karato, S. (2003, 10). Whole-mantle convection and the transition-zone water filter. *Nature*, *425*, 39–44. Retrieved from https://doi.org/10.1038/nature01918

Beyreuther, M., Barsch, R., Krischer, L., Megies, T., Behr, Y., & Wassermann, J. (2010, 06). Obspy: A python toolbox for seismology. *Seismological Research Letters*, *81*, 530–533. Retrieved from https://doi.org/10.1111/10.1785/gssrl.81.3.530

Chang, S.-J., Ferreira, A. M., Ritsema, J., van Heijst, H. J., & Woodhouse, J. H. (2014). Global radially anisotropic mantle structure from multiple datasets: A review, current challenges, and outlook. *Tectonophysics*, *617*, 1–19. Retrieved from https://doi.org/10.1016/j.tecto.2014.01.033

Chen, X., Levin, V., & Yuan, H. (2021). Small shear wave splitting delays suggest weak anisotropy in cratonic mantle lithosphere. *Geophysical Research Letters*, *48*, e2021GL093861. Retrieved from https://doi.org/10.1029/2021GL093861

Chevrot, S. (2000). Multichannel analysis of shear wave splitting. *Journal of Geophysical Research: Solid Earth*, *105*, 21579–21590. Retrieved from https://doi.org/10.1029/2000JB900199

Choy, G. L., & Richards, P. G. (1975). Pulse distortion and Hilbert transformation in multiply reflected and refracted body waves. *Bull. seism. Soc. Am.*, *65*(1), 55–70.

Cottaar, S., & Romanowicz, B. (2013). Observations of changing anisotropy across the southern margin of the African LLSVP. *Geophysical Journal International*, *195*, 1184–1195. Retrieved from https://doi.org/10.1093/gji/ggt285

Creasy, N., Long, M. D., & Ford, H. A. (2017). Deformation in the lowermost mantle beneath Australia from observations and models of seismic anisotropy. *Journal of Geophysical Research: Solid Earth*, *122*, 5243–5267. Retrieved from https://doi.org/10.1002/2016JB013901

Creasy, N., Miyagi, L., & Long, M. D. (2020). A Library of Elastic Tensors for Lowermost Mantle Seismic Anisotropy Studies and Comparison With Seismic Observations. *Geochemistry, Geophysics, Geosystems*, *21*, e2019GC008883. Retrieved from https://doi.org/10.1029/2019GC008883

Creasy, N., Pisconti, A., Long, M. D., & Thomas, C. (2021). Modeling of seismic anisotropy observations reveals plausible lowermost mantle flow directions beneath Siberia. *Geochemistry, Geophysics, Geosystems*, e2021GC009924. Retrieved from https://doi.org/10.1029/2021GC009924

Crotwell, P., Owens, T. J., & Ritsema, J. (1999). The TauP Toolkit: Flexible Seismic Travel-Time and Raypath Utilities. *Seismological Research Letters*, *70*. Retrieved from https://doi.org/10.1785/gssrl.70.2.154

Davies, D., Kelly, E. J., & Filson, J. R. (1971). Vespa process for analysis of seismic signals. *Nature*, *232*, 8–13. Retrieved from https://doi.org/10.1038/physci232008a0

Deng, J., Long, M. D., Creasy, N., Wagner, L., Beck, S., Zandt, G., ... Minaya, E. (2017). Lowermost mantle anisotropy near the eastern edge of the Pacific LLSVP: constraints from SKS-SKKS splitting intensity measurements. *Geophysical Journal International*, *210*, 774–786. Retrieved from https://doi.org/10.1093/gji/ggx190

Dziewonski, A. M., & Anderson, D. L. (1981). Preliminary reference Earth model. *Physics of the Earth and Planetary Interiors*, *25*, 297–356. Retrieved from https://doi.org/10.1016/0031-9201(81)90046-7

Eakin, C., Wirth, E., Wallace, A., Ulberg, C., Creager, K., & Abers, G. (2019). SKS Splitting beneath Mount St. Helens: Constraints on Sub-Slab Mantle Entrainment. *Geochemistry, Geophysics, Geosystems*, *20*, 4202–4217. Retrieved from https://doi.org/10.1029/2019GC008433

Ford, H. A., Long, M. D., He, X., & Lynner, C. (2015). Lowermost mantle flow at the eastern edge of the African Large Low Shear Velocity Province. *Earth and Planetary Science Letters*, *420*, 12–22. Retrieved from https://doi.org/10.1016/j.epsl.2015.03.029

Frost, D. A., & Romanowicz, B. (2021). Effects of upper mantle structure beneath Alaska on core-sensitive seismic wave absolute and differential measurements: Implications for estimates of inner core anisotropy. *Physics of the Earth and Planetary Interiors*, *315*, 106713. doi: https://doi.org/10.1016/j.pepi.2021.106713

Frost, D. A., Romanowicz, B., & Roecker, S. (2020). Upper mantle slab under Alaska: contribution to anomalous core-phase observations on south-Sandwich to Alaska paths. *Physics of the Earth and Planetary Interiors*, *299*, 106427. Retrieved from https://doi.org/10.1016/j.pepi.2020.106427

Frost, D. A., Rost, S., Selby, N., & Stuart, G. (2013). Detection of a tall ridge at the core-mantle boundary from scattered PKP energy. *Geophys. J. Int.*, *195*. Retrieved from https://doi.org/10.1093/gji/ggt242

Grund, M., & Ritter, J. R. (2018). Widespread seismic anisotropy in Earth's lowermost mantle beneath the Atlantic and Siberia. *Geology*, *47*, 123–126. Retrieved from https://doi.org/10.1130/G45514.1

Hein, G., Kolínský, P., Bianchi, I., Bokelmann, G., & Group, A. W. (2021). Shear wave splitting in the Alpine region. *Geophysical Journal International*, *227*(3), 1996-2015. Retrieved from https://doi.org/10.1093/gji/ggab305

IRIS Transportable Array. (2003). *USArray Transportable Array.* International Federation of Digital Seismograph Networks. Retrieved from https://www.fdsn.org/networks/detail/TA/ doi: 10.7914/SN/TA

Kneller, E. A., van Keken, P. E., ichiro Karato, S., & Park, J. (2005). B-type olivine fabric in the mantle wedge: Insights from high-resolution non-newtonian subduction zone models. *Earth and Planetary Science Letters*, *237*, 781–797. Retrieved from https://doi.org/10.1016/j.epsl.2005.06.049

Leng, K., Nissen-Meyer, T., & van Driel, M. (2016). Efficient global wave propagation adapted to 3-D structural complexity: a pseudospectral/spectral-element approach. *Geophysical Journal International*, *207*(3), 1700-1721. Retrieved from https://doi.org/10.1093/gji/ggw363

Leng, K., Nissen-Meyer, T., van Driel, M., Hosseini, K., & Al-Attar, D. (2019). AxiSEM3D: broad-band seismic wavefields in 3-D global earth models with undulating discontinuities. *Geophysical Journal International*, *217*(3), 2125-2146. Retrieved from https://doi.org/10.1093/gji/ggz092

Li, M., & Zhong, S. (2017). The source location of mantle plumes from 3D spherical models of mantle convection. *Earth and Planetary Science Letters*, *478*, 47–57. Retrieved from https://doi.org/10.1016/j.epsl.2017.08.033

Li, Z., Leng, K., Jenkins, J., & Cottaar, S. (2022). Kilometer-scale structure on the core–mantle boundary near hawaii. *Nature Communications*, 1–8. Retrieved from https://doi.org/10.1038/s41467-022-30502-5

Link, F., & Rümpker, G. (2021). Resolving Seismic Anisotropy of the Lithosphere–Asthenosphere in the Central/Eastern Alps Beneath the SWATH-D Network. *Frontiers in Earth Science*, *9*. Retrieved from https://doi.org/10.3389/feart.2021.679887

Liu, K., Elsheikh, A., Lemnifi, A., Purevsuren, U., Ray, M., Refayee, H., ... Gao, S. (2014). A uniform database of teleseismic shear wave splitting measurements for the western and central United States. *Geochemistry, Geophysics, Geosystems*, *15*, 2075–2085. Retrieved from https://doi.org/10.1002/2014GC005267

Long, M. D. (2009). Complex anisotropy in D" beneath the eastern Pacific from SKS–SKKS splitting discrepancies. *Earth and Planetary Science Letters*, *283*, 181-189. Retrieved from https://doi.org/10.1016/j.epsl.2009.04.019

Long, M. D. (2016). The Cascadia Paradox: Mantle flow and slab fragmentation in the Cascadia subduction system. *Journal of Geodynamics*, *102*, 151-170. Retrieved from https://doi.org/10.1016/j.jog.2016.09.006

Long, M. D., & Becker, T. (2010). Mantle dynamics and seismic anisotropy. *Earth and Planetary Science Letters*, *297*, 341–354. Retrieved from https://doi.org/10.1016/j.epsl.2010.06.036

Long, M. D., Gao, H., Klaus, A., Wagner, L. S., Fouch, M. J., James, D. E., & Humphreys, E. (2009). Shear wave splitting and the pattern of mantle flow beneath eastern Oregon. *Earth and Planetary Science Letters*, *288*(3), 359–369. Retrieved from https://doi.org/10.1016/j.epsl.2009.09.039

Long, M. D., & Lynner, C. (2015). Seismic anisotropy in the lowermost mantle near

the Perm Anomaly. *Geophysical Research Letters*, *42*, 7073–7080. Retrieved from https://doi.org/10.1002/2015GL065506

Lutz, K., Long, M., Creasy, N., & Deng, J. (2020). Seismic anisotropy in the lowermost mantle beneath North America from SKS-SKKS splitting intensity discrepancies. *Physics of the Earth and Planetary Interiors*, *305*, 106504. Retrieved from https://doi.org/10.1016/j.pepi.2020.106504

Löberich, E., Long, M. D., Wagner, L. S., Qorbani, E., & Bokelmann, G. (2021). Constraints on Olivine Deformation From SKS Shear-Wave Splitting Beneath the Southern Cascadia Subduction Zone Back-Arc. *Geochemistry, Geophysics, Geosystems*, *22*, e2021GC010091. Retrieved from https://doi.org/10.1029/2021GC010091

Marone, F., & Romanowicz, B. (2007). The depth distribution of azimuthal anisotropy in the continental upper mantle. *Nature*, *447*, 198–201. Retrieved from https://doi.org/10.1038/nature05742

Mondal, P., & Long, M. D. (2020). Strong seismic anisotropy in the deep upper mantle beneath the cascadia backarc: Constraints from probabilistic finite-frequency sks splitting intensity tomography. *Earth and Planetary Science Letters*, *539*, 116172. Retrieved from https://doi.org/10.1016/j.epsl.2020.116172

Montagner, J.-P., & Anderson, D. L. (1989). Petrological constraints on seismic anisotropy. *Physics of the Earth and Planetary Interiors*, *54*, 82–105. Retrieved from https://doi.org/10.1016/0031-9201(89)90189-1

Monteiller, V., & Chevrot, S. (2011). High-resolution imaging of the deep anisotropic structure of the San Andreas Fault system beneath southern California. *Geophysical Journal International*, *186*, 418-446. Retrieved from https://doi.org/10.1111/j.1365-246X.2011.05082.x

Niu, F., & Perez, A. M. (2004). Seismic anisotropy in the lower mantle: A comparison of waveform splitting of SKS and SKKS. *Geophysical Research Letters*, *31*. Retrieved from https://doi.org/10.1029/2004GL021196

Nowacki, A., & Wookey, J. (2016). The limits of ray theory when measuring shear wave splitting in the lowermost mantle with ScS waves. *Geophysical Journal International*, *207*, 1573–1583. Retrieved from https://doi.org/10.1093/gji/ggw358

Nowacki, A., Wookey, J., & Kendall, J.-M. (2010). Deformation of the lowermost mantle from seismic anisotropy. *Nature*, *467*, 1091–1094. Retrieved from https://doi.org/10.1038/nature09507

Nowacki, A., Wookey, J., & Kendall, J.-M. (2011). New advances in using seismic anisotropy, mineral physics and geodynamics to understand deformation in the lowermost mantle. *Journal of Geodynamics*, *52*, 205–228. Retrieved from https://doi.org/10.1016/j.jog.2011.04.003

Panning, M., & Romanowicz, B. (2006). A three-dimensional radially anisotropic model of shear velocity in the whole mantle. *Geophysical Journal International*, *167*, 361–379. Retrieved from https://doi.org/10.1111/j.1365-246X.2006.03100.x

Reiss, M., Long, M. D., & Creasy, N. (2019). Lowermost Mantle Anisotropy Beneath Africa From Differential SKS-SKKS Shear-Wave Splitting. *Journal of Geophysical Research: Solid Earth*, *124*(8), 8540–8564. Retrieved from https://doi.org/10.1029/2018JB017160

Reiss, M., & Rümpker, G. (2017). SplitRacer: MATLAB Code and GUI for Semiautomated Analysis and Interpretation of Teleseismic Shear-Wave Splitting. *Seismological Research Letters*, *88*, 392 – 409. Retrieved from https://doi.org/10.1785/0220160191

Restivo, A., & Helffrich, G. (2006). Core–mantle boundary structure investigated using SKS and SKKS polarization anomalies. *Geophysical Journal International*, *165*, 288–302. Retrieved from https://doi.org/10.1111/j.1365-246X.2006.02901.x

Rost, S., & Thomas, C. (2002). Array Seismology: Methods and Applications. *Reviews of Geophysics*, *40*(3), 1–27. Retrieved from https://doi.org/10.1029/2000RG000100

Rost, S., & Thomas, C. (2009). Improving Seismic Resolution Through Array Processing Techniques. *Surveys in Geophysics*, *30*, 271–299. Retrieved from https://doi.org/10.1007/s10712-009-9070-6

Russo, R., Gallego, A., Comte, D., Mocanu, V., Murdie, R., & VanDecar, J. (2010). Source-side shear wave splitting and upper mantle flow in the Chile Ridge subduction Region. *Geology*, *38*, 707–710. Retrieved from https://doi.org/10.1130/G30920.1

Selby, N. D. (2008). Application of a generalized F detector at a seismometer array. *Bull. seism. Soc. Am.*, *98*(5), 2469–2481. doi: 10.1785/0120070282

Silver, P. G. (1996). Seismic Anisotropy beneath the Continents: Probing the Depths of Geology. *Annual Review of Earth and Planetary Sciences*, *24*(1), 385 – 432. Retrieved from https://doi.org/10.1146/annurev.earth.24.1.385

Silver, P. G., & Chan, W. W. (1991). Shear wave splitting and subcontinental mantle deformation. *Journal of Geophysical Research: Solid Earth*, *96*, 16429–16454. Retrieved from https://doi.org/10.1029/91JB00899

Tackley, P. J. (2000). Mantle Convection and Plate Tectonics: Toward an Integrated Physical and Chemical Theory. *Science*, *288*(5473), 2002–2007. Retrieved from https://doi.org/10.1126/science.288.5473.2002

Tesoniero, A., Leng, K., Long, M. D., & Nissen-Meyer, T. (2020). Full wave sensitivity of SK(K)S phases to arbitrary anisotropy in the upper and lower mantle. *Geophysical Journal International*, *222*(1), 412 – 435. Retrieved from https://doi.org/10.1093/gji/ggaa171

Torsvik, T. (2019). Earth history: A journey in time and space from base to top. *Tectonophysics*, *760*, 297–313. Retrieved from https://doi.org/10.1016/j.tecto.2018.09.009

Trabant, C., Hutko, A. R., Bahavar, M., Karstens, R., Ahern, T., & Aster, R. (2012). Data Products at the IRIS DMC: Stepping Stones for Research and Other Applications. *Seismological Research Letters*, *83*, 846–854. doi: https://doi.org/10.1785/0220120032

van der Hilst, R., Widiyantoro, S., & Engdahl, E. (1997). Evidence for deep mantle circulation from global tomography. *Nature*, *386*, 578–584. Retrieved from https://doi.org/10.1038/386578a0

Walker, A., & Wookey, J. (2012). MSAT - a new toolkit for the analysis of elastic and seismic anisotropy. *Computers and Geosciences*, *49*, 81–90. Retrieved from https://doi.org/10.1016/j.cageo.2012.05.031

Walpole, J., Wookey, J., Masters, G., & Kendall, J. M. (2014). A uniformly processed data set of SKS shear wave splitting measurements: A global investigation of upper mantle anisotropy beneath seismic stations. *Geochemistry, Geophysics, Geosystems*, *15*, 1991–2010. Retrieved from

https://doi.org/10.1002/2014GC005278

Walsh, E., Arnold, R., & Savage, M. K. (2013). Silver and Chan revisited. *Journal of Geophysical Research: Solid Earth*, *118*, 5500–5515. Retrieved from https://doi.org/10.1002/jgrb.50386

Wang, Y., & Wen, L. (2004). Mapping the geometry and geographic distribution of a very low velocity province at the base of the Earth's mantle. *Journal of Geophysical Research: Solid Earth*, *109*. Retrieved from https://doi.org/10.1029/2003JB002674

Wessel, P., & Smith, W. H. F. (1998). New, improved version of generic mapping tools released. *Eos, Transactions American Geophysical Union*, *79*, 579–579. Retrieved from https://doi.org/10.1029/98EO00426

Wolf, J., Creasy, N., Pisconti, A., Long, M. D., & Thomas, C. (2019). An investigation of seismic anisotropy in the lowermost mantle beneath Iceland. *Geophysical Journal International*, *219*(Supplement_1), S152 – S166. Retrieved from https://doi.org/10.1093/gji/ggz312

Wolf, J., & Evans, D. A. D. (2022). Reconciling supercontinent cycle models with ancient subduction zones. *Earth and Planetary Science Letters*, 117293. Retrieved from https://doi.org/10.1016/j.epsl.2021.117293

Wolf, J., & Long, M. D. (2022). Slab-driven flow at the base of the mantle beneath the northeastern pacific ocean. *Earth and Planetary Science Letters*, *594*, 117758. Retrieved from https://doi.org/10.1016/j.epsl.2022.117758

Wolf, J., Long, M. D., Creasy, N., & Garnero, E. (in review). On the measurement of Sdiff splitting caused by lowermost mantle anisotropy. *submitted to Geophysical Journal International*.

Wolf, J., Long, M. D., Leng, K., & Nissen-Meyer, T. (2022a). Constraining deep mantle anisotropy with shear wave splitting measurements: Challenges and new measurement strategies. *Geophysical Journal International*, 507 – 527. Retrieved from https://doi.org/10.1093/gji/ggac055

Wolf, J., Long, M. D., Leng, K., & Nissen-Meyer, T. (2022b). Sensitivity of SK(K)S and ScS phases to heterogeneous anisotropy in the lowermost mantle from global wavefield simulations. *Geophysical Journal International*, *228*, 366–386. Retrieved from https://doi.org/10.1093/gji/ggab347

Wolfe, C. J., & Silver, P. G. (1998). Seismic anisotropy of oceanic upper mantle:

Shear wave splitting methodologies and observations. *Journal of Geophysical Research: Solid Earth*, *103*(B1), 749–771. Retrieved from https://doi.org/10.1029/97JB02023

Wookey, J., Kendall, J.-M., & Rümpker, G. (2005b). Lowermost mantle anisotropy beneath the north Pacific from differential S-ScS splitting. *Geophysical Journal International*, *161*, 829–838. Retrieved from https://doi.org/10.1111/j.1365-246X.2005.02623.x

Wookey, J., Stackhouse, S., Kendall, J.-M., Brodholt, J., & Price, G. (2005a). Efficacy of the Post-Perovskite Phase as an Explanation for Lowermost-Mantle Seismic Properties. *Nature*, *438*, 1004–1007. Retrieved from https://doi.org/10.1038/nature04345

Yang, B., Liu, Y., Dahm, H., Liu, K., & Gao, S. (2017). Seismic azimuthal anisotropy beneath the eastern United States and its geodynamic implications. *Geophysical Research Letters*, 2670–2678. Retrieved from https://doi.org/10.1002/2016GL071227